HHS Public Access

Author manuscript

NMR Biomed. Author manuscript; available in PMC 2023 October 01.

Published in final edited form as:

NMR Biomed. 2023 June ; 36(6): e4715. doi:10.1002/nbm.4715.

A snapshot of the vast array of diamagnetic CEST MRI contrast agents

Dario Livio Longo[1], **Antonella Carella**[1], **Alessia Corrado**[1], **Elisa Pirotta**[1], **Zinia Mohanta**[2,3], **Aruna Singh**[2,3], **Julia Stabinska**[2,3], **Guanshu Liu**[2,3], **Michael T. McMahon**[2,3]

[1]Institute of Biostructures and Bioimaging (IBB), National Research Council of Italy (CNR), Turin, Italy

[2]F.M. Kirby Center for Functional Brain Imaging, Kennedy Krieger Institute, Baltimore, Maryland, USA

[3]Department of Radiology, Johns Hopkins University School of Medicine, Baltimore, Maryland, USA

Abstract

Since the inception of CEST MRI in the 1990s, a number of compounds have been identified as suitable for generating contrast, including paramagnetic lanthanide complexes, hyperpolarized atom cages and, most interesting, diamagnetic compounds. In the past two decades, there has been a major emphasis in this field on the identification and application of diamagnetic compounds that have suitable biosafety profiles for usage in medical applications. Even in the past five years there has been a tremendous growth in their numbers, with more and more emphasis being placed on finding those that can be ultimately used for patient studies on clinical 3 T scanners. At this point, a number of endogenous compounds present in tissue have been identified, and also natural and synthetic organic compounds that can be administered to highlight pathology via CEST imaging. Here we will provide a very extensive snapshot of the types of diamagnetic compound that can generate CEST MRI contrast, together with guidance on their utility on typical preclinical and clinical scanners and a review of the applications that might benefit the most from this new technology.

1 | INTRODUCTION

A core feature of chemical exchange saturation transfer (CEST) imaging is the capability of amplifying the signal from low-concentration diamagnetic compounds through their interactions with water, thus enabling their detection at higher spatial resolution than with conventional spectroscopic methods. Additionally, this signal amplification is based on continuous transfer of saturation between protons in specific molecules and water protons, achieved by simply adding a frequency-selective presaturation pulse to an imaging sequence. Furthermore, the exchange of spins is dependent on several environmental factors

Correspondence: Dario Livio Longo, Institute of Biostructures and Bioimaging (IBB), National Research Council of Italy (CNR), Via Nizza 52, 10126 Torino, Italy. dariolivio.longo@cnr.it, Guanshu Liu and Michael T. McMahon, F.M. Kirby Center for Functional Brain Imaging, Kennedy Krieger Institute, Baltimore, MD, USA. gliu10@jhmi.edu and mcmahon@kennedykrieger.org.

including temperature and pH, enabling insight into these parameters through measurement of contrast. CEST imaging can be performed on standard clinical MRI scanners without hardware modifications. For CEST MRI to become a widely used technology within radiology departments, a major need is to identify which compounds can be detected in the tissues of interest. Most CEST applications focus on endogenous molecules that can be found in the human body, or chemical substances that can be administrated externally to generate exogenous CEST contrast. In general, CEST agents can be divided into three groups based on their composition. Paramagnetic CEST agents (paraCEST) contain metallic ions that induce large labile proton chemical shifts and with bound water and other labile proton sites shifted by up to 600 ppm from water.[1–5] ParaCEST agents can be detected at high amplification factors via saturation transfer due to the extension of the slow exchange regime to higher chemical exchange rates, and also have the advantage that the exchange properties of these complexes can respond to various metabolites, rendering them excellent as environmental sensors. Hyperpolarized CEST agents (hyperCEST) are molecular cages,[6,7] metal–organic frameworks[8,9] or macromolecular host structures[10,11] that can entrap hyperpolarized ^{129}Xe in such a way that these atoms have large chemical shifts compared with free ^{29}Xe in water yet can exchange rapidly out of the host structure. Diamagnetic chemical CEST agents (diaCEST) are diamagnetic compounds that are either naturally occurring compounds or synthetic contrast agents with exchangeable protons, i.e., −OH, $-NH_2$, −NH, with chemical shifts within 14 ppm from water. Because of their excellent biocompatibility and biodegradability, a number of diaCEST agents and their potential applications have been widely investigated and reported in multiple preclinical and clinical studies. As a result, the list of diaCEST probes that could potentially be used in clinical settings has grown tremendously since the seminal works of Balaban, van Zijl and colleagues[12–17] and our previous diaCEST agent review.[18] The purpose of this review is to provide an updated overview of the various types of diamagnetic compound suitable for molecular imaging in the context of their suitability for clinical CEST MRI applications. We do not extensively discuss endogenous CEST agents, which have been described in other review articles in this *NMR in Biomedicine* issue. Instead we focus on exogenous diaCEST probes, which are particularly promising candidates for clinical translation because of their safety profiles and potential to highlight a wide range of pathologies.

2 | SMALL MOLECULES

2.1 | Sugars

Glucose is a key marker of the dysregulated metabolism in solid tumors. Consequently, imaging-based approaches that allow us to detect the increased glucose uptake in cancer cells are needed to improve cancer diagnosis. Positron emission tomography (PET) imaging of glucose relies on the use of radiolabeled ^{18}F-fluoro-2-deoxy-2-D-glucose (FDG) and nowadays is considered the gold standard for detecting the upregulated glucose metabolism found in malignancies. However, despite the high specificity of FDG-PET for tumor detection, PET or PET/CT (computed tomography) has limits for diagnostic value due to (i) lower sensitivity of PET in comparison to MRI (63–93% versus 89–100%), especially for small lesions,[19] and (ii) insufficient anatomic details provided by CT.[20] This has prompted a quest for alternatives to radiolabeled glucose. Recently, the CEST technique

has been proposed to detect exogenously administered, unlabeled glucose and a variety of its analogues (glucoCEST).[21–23]

D-glucose was first investigated as potential alternative to FDG owing to its molecular structure possessing a large number of labile hydroxyl protons reflected between 1 and 2 ppm in *z* spectra (Figure 1A) and its use in the clinic, including intravenous infusion for glucose tolerance testing.[24] In vivo studies on two human breast cancer murine models (MDA-MB-231 and MCF-7) demonstrated the detectability of this molecule using CEST MRI and showed the capability to discriminate between different tumor phenotypes based on the differences in measured glucoCEST contrast.[23] Similar results were observed by Walker-Samuel and coworkers on two subcutaneous human colorectal tumor mouse models (LS174T and SW1222 cancer cells), with the glucoCEST contrast correlating well with the FDG-PET findings. In addition, this study highlighted that the measured glucoCEST contrast might report not only on cellular uptake and metabolic activity but also on the vascular delivery of glucose, thus increasing the complexity of the origin of the observed contrast.[22] Studies are ongoing to shed light on the source of the observed glucoCEST contrast (Figure 1B). Glucose proton exchange can be modeled using four pools and is pH dependent,[25] which also adds complexity to the origin of the observed contrast, since tumor extracellular pH (pH_e) is typically acidic. To date, only one study, by Capozza and coworkers, has compared the glucoCEST contrast with FDG-PET for monitoring tumor response to therapy. In this study, the response of glucoCEST contrast was monitored in mice bearing 4T1 breast tumor treated with two different therapeutics, doxorubicin and dichloroacetate. Doxorubicin treatment resulted in a reduced tumor volume compared with untreated, which was observable 5 d after treatment, and a 1.5% drop in glucoCEST contrast at 14 d after treatment, whereas the FDG-PET is not able to report on any difference (Figure 1C).[26]

D-glucose can be metabolized; therefore, analogues of this molecule have been investigated as non-metabolizable alternatives. Rivlin et al. considered 3-*O*-methyl-D-glucose (3OMG), a synthetic non-toxic and non-metabolizable derivative of glucose. Since the 3OMG uptake and entrapment inside the cancer cells is comparable to that of the FDG molecule, they observed a marked and prolonged glucoCEST contrast in several murine tumor models.[27] However, when native D-glucose and 3OMG were compared side by side for the same experimental conditions, administered doses and tumor model, they provided similar glucoCEST contrasts, even with their different metabolic fates.[28] Another sugar, xylose, can maintain high concentration in tissues because of its slow metabolism. Furthermore, it is able to pass through the blood–brain barrier (BBB). Wang and coworkers demonstrated in vivo that glucoCEST contrast could be detected upon bolus injection of xylose in rat brain.[29] Another non-metabolizable glucose derivative, 2-DG, was detectable in the brain of healthy rats, although the lower safety profile of this molecule poses some challenges for the high doses required by the CEST technique.[30] Maltitol, a non-metabolizable sugar, was investigated in vivo and demonstrated a moderate accumulation and glucoCEST contrast in the extracellular space of rat gliomas (change in asymmetric magnetization transfer ratio, $\Delta MTR_{asym} \sim 1.6\%$) without showing appreciable uptake in healthy brain tissue.[31] Myo-inositol is another sugar that has displayed promise as well.[32]

2.2 | Amino acids, creatine and nucleic acids

Amino acids are key building blocks for proteins and are vital for various processes including skeletal muscle function, atrophy and tumor growth. They also play key roles in cell signaling, cell homeostasis, gene expression and a number of important pathways. Therefore, amino acid detection could reveal quite a bit about pathology. There are a number of labile protons on the 20 natural amino acids that might be exploitable for CEST studies. Their detection was envisioned in the earlier works of Balaban and colleagues[15]; however, more recently investigators have focused on glutamate, arginine and alanine which are readily detected and can be also present at millimolar concentrations in tissue.[33–36] For example, it was discovered that glutamate possessed amine protons that are relatively slow compared with those of other amino acids, enabling glutamate CEST (GluCEST) detection after infusion.[35] This probe is present at millimolar concentrations in the brain, allowing the use of GluCEST for detecting elevated concentrations in the striatum and motor cortex in a mouse model of dopamine deficiency.[37] This probe may also hold promise for epilepsy and other pathologies,[38,39] and is the subject of a review later in this issue. Alanine is also present at millimolar concentrations in tissue and has suitable exchange rates for detection.[33,40] Arginine possesses guanidyl amine protons that are well suited for detection, and this agent has been used for a few different types of exogenous contrast application. For example, pH sensors were built around arginine into hydrogels suitable for transplantation of cells to monitor their location and their survival.[41] Creatine is synthesized from the amino acids glycine and arginine, and also possesses guanidyl protons well suited for detection and present at high concentrations in skeletal muscle, along with its phosphorylated derivative phosphocreatine.[42–46] It is also a common nutritional supplement that can be detected after administration.[47] Further discussion of this agent can be found in a later review in this issue. Cytosine is a natural nucleic acid detectable through CEST contrast,[48] as are its derivatives such as 5-fluorocytosine[48] and deoxycytidine.[49] Thymidine is another that is not as well detected; however, Bar-Shir and his colleagues showed that chemically modified thymidine compounds provide a favorable CEST signal at about 5 ppm, attributed to pyrimidine amino protons, at physiological pH. Furthermore, another cytosine analog, gemcitabine, has two strong CEST MRI signals at physiological conditions (pH = 7.4 and 37 °C, phosphate buffered saline (PBS)), i.e., 2.2 ppm and 1.0 ppm, corresponding to the amino and hydroxyl protons, respectively.[50]

2.3 | Porphyrin metabolites

Porphyrin biosynthesis is an important pathway that is involved in a number of biological processes including angiogenesis. As the porphyrins are also one of the most aromatic compounds produced by the body with large ring currents, it was expected that these could also possess excellent CEST properties as well. The inner ring NH protons are labile and can be tuned to maximize CEST contrast depending on the substitution of the porphyrin ring, as we have shown recently.[51] These are highly upfield shifted, resonating at about 16 ppm higher field than NH resonances on lysine rich peptides, with these unusual shifts due to the effect of “ring currents” formed by the precession of 18 π-electrons in the porphyrin ring. A series of natural porphyrins and a few artificial porphyrins were tested, with the substitution of the porphyrin ring impacting the exchange properties quite substantially. Other artificial porphyrins appear promising as well.[52] Porphyrins might present unique challenges for in

vivo imaging studies, as they tend to ligate metals at their axial site and self-aggregate. However, they might also present unique opportunities for medical applications such as combining MRI with optical image-guidance of surgeries[53] and photodynamic therapies[54] that employ similar compounds.

2.4 | Pharmaceutical excipients

Pharmaceutical excipients should be molecules endowed with high or very high safety profiles, making these interesting prospects based on the high concentrations often needed by CEST agents for in vivo detection. Longo and coworkers performed in vivo experiments on murine breast (TS/A) and melanoma (B16) tumor models on a wide range of excipients, with meglumine, *N*-acetyl glucosamine and ascorbic acid yielding the highest CEST contrast enhancement.[55]

2.5 | Salicylates, anthranilates and analogs

We discovered that many salicylates and anthranilates can act as high-performance CEST agents, with their CEST properties tuned through intramolecular hydrogen bonding.[56–58] We have characterized a number of these compounds, which possess labile protons with chemical shifts between 5 and 12 ppm from water, including the ones shown in Figure 2, and with chemical exchange rates (k_{ex}) = 100–5000 s^{-1}, allowing outstanding detection sensitivity for a variety of magnetic field strengths. It is also possible to derivatize the anthranilates and still retain large chemical shifts on the labile protons, with hydrazo-CEST probes being one example.[59,60] Acetanilides are similar compounds, which form intermolecular hydrogen bonds, resulting in well tuned k_{ex}.[61] Since the labile protons resonate more than 4 ppm from water, there is minimal overlap with endogenous CEST agents, which should maximize the potential for quantification. Another attractive feature of salicylate and anthranilate agents is the wealth of literature on pharmacokinetics and toxicity.

2.6 | Triiodobenzene pH imaging agents

Iodinated X-ray/CT contrast agents have been thoroughly investigated for CEST MRI due to their larger shifted amide protons and to their very high safety profiles, even at high doses.[63] In recent years, several iodinated molecules, including iopamidol, iobitridol, iodixanol, iopromide and iohexol have demonstrated excellent results in terms of MRI-CEST contrast efficiency and as pH responsive contrast agents. In particular, the development of contrast agents able to report on tissue pH is of clinical relevance, since several pathologies are associated with an altered acid–base balance, including ischemia, renal failure and cancer.[64–67] The exploitation of iodinated contrast agents as MRI-based contrast agents was proposed by Aime and coworkers first as T_2 exchange agents[68] and then as demonstrating interesting MRI-CEST properties in vitro with the use of iopamidol.[69] A further step was provided by Longo and coworkers by exploiting the two not chemically equivalent amide groups of iopamidol for a concentration-independent ratiometric approach to provide pH responsiveness in the physiological pH range, and demonstrating in vivo the capability to obtain highly spatially resolved pH maps in the murine kidneys at high magnetic field strengths (7 T).[70] A throughout characterization of the pH responsive properties of iopamidol was performed by Sun et al., showing high accuracy in the pH range between

6.0 and 7.5 even at moderately high fields (4.7 T, Figure 3A).[71] Later on, Longo et al. demonstrated tumor pH_e mapping with the use of iopamidol.[72] In addition, they proposed a novel approach for pH mapping even for molecules endowed with only one exchanging proton, such as iobitridol (a non-ionic, monomeric, low-osmolar iodinated contrast medium), by exploiting the ratio of two different RF irradiation power levels (Figure 3). This novel approach provided pH values comparable to those provided by iopamidol in both tumor and renal pH images. In the same time period, Pagel et al. showed that iopromide, a low-osmolar, non-ionic iodinated contrast medium with a similar chemical structure to iopamidol, can be exploited as a pH responsive contrast agent for mapping tissue pH, dubbing the approach acidoCEST (Figure 3C).[73] The comparison of iopromide and iopamidol as pH responsive agents showed that iopromide can produce a pH measurement with a higher dynamic range, whereas iopamidol can produce a more precise pH measurement, although the calculated pH values were not significantly different.[74] In another study, Wu et al. applied multi-pool Lorentzian fitting to resolve multiple and partially overlapping CEST signals in the kidney and generalized the dual RF power-based ratiometric approach by ratioing the resolved saturation transfer effects measured at two different power levels and frequency offsets.[75] As a result of these improvements, the pH detection range of iopamidol-based CEST MRI at 4.7 T could be extended.

Iodixanol, a dimeric iso-osmolar, non-ionic, iodinated radiocontrast agent, was exploited by Arena and collaborators, showing another ratiometric approach for pH imaging without the need for two different resonant frequencies or of a continuous-wave irradiation when using a double-angle pulsed saturation scheme.[76] Recently, also iohexol, another iodinated, non-ionic, low-osmolar contrast agent, was investigated within the spin-lock approach as a competitive method for generating contrast in comparison with the CEST one.[77] Most of these contrast media have been compared in vivo upon extravasation and accumulation in the extracellular space in tumors for their efficiency to generate MRI-CEST contrast in respect to the CT attenuation properties. Overall, a comparable CEST contrast was observed among all the investigated molecules, with a strong and positive correlation between CT and CEST-MRI derived contrast enhancement.[78]

Over the years, gadolinium has always been considered the gold standard in the MRI contrast enhanced approach, although serious clinical issues have been identified, including contraindicating Gd-enhanced MRI for patients with poor kidney function due to risk of developing nephrogenic systemic fibrosis[79,80] and Gd-contrast agents accumulating in several organs over many years.[81–84] Iodinated contrast media are an alternative that has been investigated using the MRI-CEST approach. In a recent study, Anemone et al. demonstrated similar pharmacokinetic profiles and contrast enhancement properties between Gd-based and iodinated molecules, with a T_1-weighted or CEST technique, respectively.[85] Interestingly, after intravenous injection, several iodinated agents showed similar perfusion properties within a breast tumor murine model, with a marked correlation in both contrast and spatial enhancement and spatial shown by iopamidol.

2.7 | Imidazole pH imaging agents

Heterocycles such as imidazole and its analogues can have highly shifted labile protons due to the presence of π-electrons and a capacity for intramolecular hydrogen bonding. These chemical features endow these compounds with NMR properties that are pH responsive. For instance, certain *N*-alkylated imidazoles, including 2-imidazole-1-yl-3-ethoxy-carbonyl propionic acid (IEPA) and 2-imidazole-1-yl-succinic acid (ISUCA), have been found to be important MRS pH sensing agents owing to the chemical shift of the C-2 proton.[86,87] We investigated various imidazole analogues and compared their N–H exchangeable protons for pH sensing by implementing CEST. Free imidazole (**1** in Figure 4) does not provide CEST contrast at neutral pH due to its fast exchange rate with water. Based on the knowledge that histidines in the catalytic site of serine proteases showed a decreased exchange rate of the imidazole N–H groups and chemical shifts as far as 13 ppm downfield from water by virtue of their hydrogen bonding network,[89,90] we decided to try and prepare an imidazole compound with a suitable intramolecular hydrogen bonding as a CEST agent. We have synthesized and tested over 25 variants at this point, and have found 4,5-bis[(Glu)carbonyl]-^{1}H-imidazole (I45DC-diGlu, **5** in Figure 4), which generates strong CEST contrast at 7.5 ppm at neutral pH.[88] The number of nitrogens in the ring and substituents attached to this were critical for stabilizing the conformation and enabling CEST contrast production.[91,92] Moreover, the two labile proton types in this molecule, high pH sensitivity and water solubility make it a good candidate for ratiometric pH measurements. The mechanism of contrast enhancement is expected to be similar to the behavior seen previously and attributed to changes in conformation as the pH drops.[91] We have tested this agent in vivo and successfully mapped the pH of mouse kidneys.[88] The imidazoles are generally considered to be well tolerated, enabling their usage in the clinic, with similar compounds such as flumizole, dacarbazine and cimetidine and a number of others having LD50s of 500–2500 mg/kg and used as anti-inflammatories, H2 antagonists, anticancer drugs, anticonvulsants, antifungals or to treat hypertension.[93,94] This combination of factors has inspired us to further test our imidazole agent for pH mapping in certain renal diseases and injuries, including those due to urinary tract obstruction and methyl malonic acidemia, with this work ongoing.

3 | MACROMOLECULES AND SUPERSTRUCTURES

3.1 | Dextran and glycogen

Small molecules possess few labile protons per molecule, and thus limited efficiency in generating CEST contrast. To overcome this limitation, macromolecules and superstructures have been explored to substantially boost the sensitivity of CEST MRI, as macromolecule and nanosized systems can be encapsulated or conjugated with a larger number of exchangeable protons. In this context, a few polysaccharides have been studied as diaCEST agents, including dextran,[95,96] glycogen,[97,98] starch[99] and other sugar-based polymers.[100] Similarly to monosaccharides such as glucose, polysaccharides also have a strong CEST signal at around 1 ppm, attributed to hydroxyl protons. Our group has extensively developed dextran as a CEST agent. Dextran is considered as an ideal polymeric CEST agent because dextrans are biologically inert and have been used in the clinic for many decades. Dextrans are also available in different sizes, permitting them to be used in

different biomedical applications, such as size-dependent tumor vascular permeability.[95] Intravenously administrated large dextrans (e.g., 150 kDa) were exploited as intravascular agents because they are restricted in the blood circulation.[101] Another recent study also showed the ability of dynamic contrast-enhanced CEST MRI to detect BBB disruption associated with brain tumors, in which a low-MW (1 kDa) dextran was used as the imaging agent.[102] General speaking, dextrans of smaller size are more suitable as an imaging moiety to construct targeted CEST MRI agents because they more easily permeate to the tumor parenchyma.[96,103] Another good example is the dextran-based prostate-specific membrane antigen (PSMA) receptor imaging that we have developed and demonstrated in experimental prostate tumors (Figure 5).[96] A micromolar detectability was accomplished to detect about 5×10^6 PSMA receptors per tumor cell, which is almost impossible for small molecular MRI agents.

Of note, recent studies have shown that the relayed Overhauser effect (rNOE) effect may also be utilized to detect polysaccharides such as glycogen by their macromolecule nature in addition to the CEST signal at 1 ppm (OH protons). In particular, the saturation on glycogen aliphatic protons is transferred to a neighboring hydroxyl proton and subsequently to water via proton chemical exchange between glycogen hydroxyl protons and water.[98,104] Such an approach enables non-invasive mapping of glycogen using a more distinguishable, pH insensitive CEST MRI signal.

To accelerate towards potential clinical translation, Consolino and collaborators have focused on the FDA-approved plasma volume expanders as macromolecular CEST agents. Both dextran 70 and Voluven showed in vivo a marked CEST contrast in a breast tumor murine model, with comparable contrast enhancement properties to that observed with a blood-pool gadolinium-based contrast agent.[99]

3.2 | Liposomes and hydrogels

Another strategy is based on the encapsulation of high payloads of diaCEST agents into liposomes or other superstructures. Our first attempt included encapsulating poly-L-Lysine, L-arginine and glycogen followed by injecting these into the footpads of mice to monitor their delivery to popliteal lymph nodes through the lymphatic system.[34] We have also developed a barbituric acid (BA) liposome (BAL) with CEST contrast at 5.0 ppm and have tested this both for monitoring intravenous delivery to colon tumors[105] and for vaginal distribution and retention.[106] BA has also been dispersed in hydrogels with contrast at 5.0 ppm and −3.4 ppm, which are related to the amount of liposomal drug (BA) and to the amount of hydrogel following hydrogel transplantation into the tumor area.[107] To overcome the sensitivity limitations of the glucoCEST approach, liposomes entrapped with glucose or 2DG have been investigated, too. The observed results demonstrated that the encapsulation into the liposomes can lower the fast chemical exchange rate of the hydroxylic protons and thus provide high glucoCEST contrast.[108] Recently, we also demonstrated the CEST MRI detection of liposomes encapsulated with gemcitabine,[50] citicoline[109] and iodixanol.[110]

Suprastructures such as hydrogels have been considered and can be detected via the large number of exchanging protons. Such systems can be exploited to deliver anticancer drugs such as pemetrexed and to monitor their accumulation within the tumor, acting as a

theranostic agent.[111] Hydrogels are also widely used as biological scaffolds to repair soft tissues after injuries; the hydrogels' in vivo distribution, biodegradation and cell survival can be monitored over time by looking at the CEST contrast, as demonstrated after implantation of hepatocytes into mice and comparing with bioluminescence reporter gene expression,[41] and also implanting these into the stroke cavity in a rat model.[112]

3.3 | Polynucleotides, poly(amino acids) and peptides

Some of the earliest work on CEST agents involved the identification of macromolecules that work well as CEST agents, including the seminal work by van Zijl and colleagues.[14] The first identified included the poly(amidoamine) dendrimer and poly-L-lysine, which possess amine and amide protons well tuned for detection between 3 and 3.5 ppm from water. More recently, salicylate-based dendrimers have been prepared with superior chemical exchange properties.[113] Polynucleotides can also possess excellent properties for detection, depending on their nucleotide sequences.[16] Furthermore, a wide range of peptide CEST agents have been designed at this point, including lysine rich protein[114] and arginine rich and threonine rich peptides.[115] Due to the outstanding promise displayed by these agents, the many variations will be covered extensively by Gilad and others in another review in this issue.

4 | APPLICATIONS OF PH IMAGING AGENTS

MRI is one of the primary means to measure tissue pH, and can be used to assess the intra- and/or extracellular tissue pH.[116] Proton exchange is particularly sensitive to the acid–base equilibrium; in fact, Balaban and co-workers reported CEST agents (shortly after the initial discovery) as pH sensors. Both paraCEST agents[117–123] and diaCEST[41,69,124–129] agents have been reported as pH sensors. Multi-color detection is an important advantage of CEST agents for pH imaging, as this allows use of ratiometric imaging to compensate for changes in agent concentration.[124] As mentioned in Section 1, two classes of diaCEST agent have shown promise for ratiometric pH mapping: the triiodobenzenes and the imidazoles, which perform well for this purpose.

One of the main focuses of pH mapping studies is applying these for cancer imaging because of the well known tumor extracellular acidification upon the combined effects of dysregulated metabolism, hypoxia and reduced perfusion.[65,66,130,131] Indeed, a number of early studies were performed to characterize the pH of tumors using CEST MRI.[67,73,74] A first in vivo demonstration of the relationship between upregulated glycolysis and tumor acidosis via CEST imaging was provided by Longo and coworkers, reporting a strong correlation between ^{18}F-FDG uptake and tumor pH_e by combining PET and MRI-CEST pH imaging in a breast tumor murine model.[132] Nowadays, high-resolution tumor pH maps are achievable within a reasonable acquisition time that allows us to obtain information on spatial tumor pH heterogeneity (Figure 6). Tumor pH_e mapping can be exploited to assess response to anticancer therapies that can alter the homeostasis of tumor acidosis. Drugs targeting the glycolytic metabolism are expected to affect the extracellular tumor acidification.[133] This has been shown in vivo in a breast cancer murine model upon dichloroacetate administration, which can revert the dysregulated glycolysis. Interestingly,

tumor pH values increase strongly after dichloroacetate treatment, confirmed by the decrease of the lactate levels, showing the early response to treatment. However, 15 d after the tumor became resistant, lactate levels were similar between untreated and treated groups and tumor pH imaging demonstrated the onset of resistance to the drug.[134] CEST pH imaging was also exploited to evaluate, in combination with FDG-PET studies, the early response to metformin on a preclinical model of pancreatic cancer.[135] However, although CEST-MRI did not report any increase in tumor pH_e, likely reflecting the mechanism of action of metformin, the subsequent PET analyses detected a reduction in glucose uptake. Since tumor acidosis is nowadays considered one of the leading causes of cancer aggressiveness and invasiveness, MRI-CEST pH imaging has been investigated as a potential imaging biomarker of the metastatic potential. Anemone and colleagues investigated several breast cancer cell lines with different metastatic potentials, showing that cell lines with higher invasiveness (larger, and higher number of lung metastases) reflected an increased tumor acidity and heterogeneity, whereas less aggressive tumors resulted in lower tumor acidosis and smaller and reduced lung metastases (Figure 7).[136] Iopamidol CEST pH imaging has also been exploited to confirm the presence of acidic niches in lymph nodes, providing precious information about the physiological microenvironment and its influence in immune cell activation and glycolytic metabolism maintenance.[137] In addition, Jones and colleagues provided the clinical translation proof of iopamidol-based pH_e mapping by measuring pH_e values in ovarian and in breast cancer patients with a clinical MRI 3 T scanner.[138] Overall, these results highlight that iopamidol-based tumor pH imaging can be considered useful for characterizing tumor aggressiveness and to assess response to anticancer therapies.

The acid–base balance plays a fundamental role in the kidneys; consequently, pH imaging of kidneys is expected to provide useful information regarding renal functionality. Some of the first evidence of altered renal pH values in a preclinical severe but transient acute kidney renal injury model were provided by Longo et al., showing marked pH alterations that restored to normal basal pH values after a recovery period.[139] In another study, upon single-kidney ischemia–reperfusion injury, iopamidol-based renal pH imaging was capable to distinguish between the clamped and the contralateral kidneys and to monitor the renal pH evolution in a moderate and in a severe injury model.[140] Additionally, Irrera and coworkers reported a dynamic CEST approach for assessing both renal perfusion and pH homeostasis in an acute ischemia–reperfusion injury murine model. Iopamidol was injected and exploited for providing a dual reading of both perfusion and pH, with a marked reduction of renal filtration and increased pH values for the clamped kidneys in comparison to the contralateral ones.[141] Consequently, the dynamic CEST approach was able to assess and distinguish the renal function between the healthy and the clamped kidneys, and these results correlated with the perfusion values obtained with a dynamic contrast enhanced (DCE)-MRI approach upon gadolinium-based contrast agent injection in the same mice. Another study tested iopamidol-based perfusion and pH maps for differentiating healthy kidneys from mild and severe chronic kidney disease in a transgenic mouse model of methyl malonic acidemia.[142] Three metrics were found to correlate with mouse weight, including contrast magnitude, filtration fraction and range in pH values across the kidneys (Figure 8). Based on the promise displayed, a pilot study of iopamidol-based quantitative pH imaging was performed by Müller-Lutz and colleagues in 2013, by measuring in vivo the pH in the bladder of a

healthy volunteer with a clinical 3 T scanner and showing a good agreement with the urine pH measured by a pH-meter.[143] In addition, the first map of kidney pH was published from a healthy subject at 3 T, showing the feasibility of this approach for translational studies.[144]

5 | ENZYME RESPONSIVE AGENTS

There are a number of probes that after administration can be altered by key enzymes to highlight pathology, particularly tumor tissue. CEST MRI has been extensively explored for detecting enzymatic activity using CEST agents that are responsive to a particular enzyme. Because very often an enzyme catalyzes biochemical reactions that involve the change of chemical groups comprised of exchangeable protons, enzymatic activity (i.e., the conversion from a substrate to a product) will result in CEST signal changes. Compared with other MRI methods, CEST MRI is advantageous because one can use a variety of bioorganic agents, even the natural substrates, as imaging probes. We first demonstrated the use of cytosine as a CEST agent to probe the enzymatic activity of cytosine deaminase (CDase).[48] When cytosine is converted to uracil by CDase, the CEST signal at about 2 ppm (aniline protons) decreases to an extent that is proportional to CDase activity. Following this study, we also successfully developed CEST MRI methods for detecting protein kinase A[145] and deoxycytidine kinase.[49] Using natural compounds to probe enzyme activity provides an efficient way to detect an enzyme without much disturbance to normal cell systems. This strategy was soon implemented by many other research groups to detect, for example, carboxypeptidase G2[146] and protease.[147] These studies imply that it is feasible to use the inherently insensitive MRI to detect a low concentration of enzymes in living subjects non-invasively.

Natural compounds typically have small CEST offsets that overlap with endogenous CEST signals (i.e., 1–4 ppm), reducing the detection specificity. To overcome this challenge, much effort has been made to develop synthetic agents with large CEST offsets to improve the specificity of enzyme detection. For instance, Bar-Shir and his colleagues employed chemically modified thymidine analogs with favorable CEST signals at about 5 ppm to detect herpes simplex virus type-1 thymidine kinase (HSV1-TK).[148,149] Using salicylic acid (~8–10 ppm)[150] as a building block, Pagel et al. developed a variety of sophisticated enzyme responsive agents, which typically have two or more well separated CEST signals, for detecting alkaline phosphatase,[151] sulfatase and esterase,[152] cathepsin B,[153] urokinase,[154] γ-glutamyl transferase (GGT)[155] and kallikrein 6 (KLK6),[156] collectively named catalyCEST (catalysis CEST) MRI.

Beyond the detection of enzymatic activity, such an approach can also be integrated into targeted therapy to obtain enzyme-specific theranostics. We have also conjugated olsalazine (Olsa), an anticancer drug with a CEST signal at 9.8 ppm, to a cell-penetrating peptide (RVRR) to construct a theranostic system (Olsa–RVRR) that is responsive to furin, an enzyme highly expressed in many aggressive tumors. Olsa–RVRR is reduced by glutathione (GSH) and cleaved by furin in the cytoplasm of cancer cells, resulting in the cleaved Olsa peptide that spontaneously self-assembles to nanostructures through intermolecular interactions (Figure 9). The self-assembled nanostructures can prevent Olsa from rapid

efflux and consequently not only increase the anti-tumor effect significantly but also lead to strong CEST signal at 9.8 ppm.

The CEST principle is also applicable to the detection of molecular binding without a synthetic metallic label. In this context, Yadav et al. first demonstrated the MRI detection of non-exchangeable aliphatic protons upon their binding to ligands.[158] In this so-called IMMOBILISE (Imaging of Molecular Binding using Ligand Immobilization and Saturation Exchange) method, aliphatic protons in a free substrate with narrow resonance NMR signal were first selectively labeled using RF pulses; if the substrate binds to the solid-like target, such as cell membrane receptors, fast magnetic transfer of the magnetic labels occurs between the labeled protons in the free substrate and those in the target backbone, followed by proton exchange between solid-like target and water. This cascade of events ultimately leads to substantial changes in water protons, which can be detected with MRI. In Yadav's study, caffeine was chosen as the model compound because caffeine is known to be a substrate for adenosine receptor A1 in the brain. The combined effects of continuous labeling (label pumping), dynamic reversible binding and water detection can generate highly enhanced detection sensitivity. For example, phantom data showed that 5 mM caffeine could result in a 4% water signal, an approximately 900-fold signal enhancement. In the mouse brain, they estimated that 2.3 mM caffeine in the blood 5 min after the infusion of 50 μL of 100 mM caffeine could generate 1–3% changes in water signal.

Generally speaking, dynamic processes for host–guest systems can be described by the exchange between host-free and host-bound states. In analog to proton exchange, the dynamic exchange of a compound between different binding states can be detected using the CEST principle with greatly enhanced sensitivity. Bar-Shir and his colleagues have successfully developed a series of fluorinated agents that enable guest exchange saturation transfer (GEST) imaging of metal ions[159,160] and non-metal ions hosted by receptors[161] For an in-depth discussion of how ^{19}F-GEST MRI can be used to study host–guest interactions, the interested reader is referred to a recent review by Avram and Bar-Shir.[162]

6 | THERANOSTICS

The use of theranostics represents a strategy to integrate imaging into drug treatment,[163–165] and is an emerging approach for carrying out targeted and individualized therapies for various diseases. In the last decade, numerous theranostic systems have been reported for the simultaneous detection and treatment of diseases by specific biomarkers or monitoring the delivery and release of drugs in real time.[166] In most of these studies, the theranostic systems were constructed in such a way that imaging probes are integrated into drug delivery carriers, either chemically or physically. While this approach has been successfully demonstrated in many preclinical studies, it poses a potential shortcoming: the addition of imaging probes will unavoidably influence the pharmacokinetics of the drug delivery systems, not to mention that this may also result in false signal if the imaging probes disassociate from the delivery systems in vivo. Hence, it is highly desirable to construct theranostic systems without imaging labels, so-called label-free theranostics. In this regard, CEST MRI has been exploited to make otherwise MRI invisible drugs imageable. This is because many drugs possess exchangeable protons that are detectable in CEST MRI. By

screening a library of anticancer drugs, our group first showed that many chemotherapeutic agents, including pyrimidine analogs, purine analogs and antifolates, can generate CEST MRI contrast, permitting detection of these label-free theranostics.[50] In the study, we demonstrated the CEST MRI detection of uptake and distribution of an i.v.-injected liposomal form of gemcitabine (a first-line anticancer drug for pancreatic cancers) in experimental tumors in mice. The detection sensitivity was estimated to be less than 1 mM for PBS samples and 1–2 mM for gel samples, suggesting that CEST MRI has a moderate sensitivity in detecting these drugs, which however still has potential in the scenarios where drugs are administered at a relatively high dose. While most CEST MRI studies were conducted using high-field scanners, a recent study[167] has shown that CEST MRI could detect gemcitabine that was loaded in hydrogel at 3 T, confirming the feasibility of using CEST MRI to detect drugs at low magnetic fields.

Non-steroidal anti-inflammatory drugs (NSAIDs) are in widespread use for the reduction of pain and inflammation. For example, one known NSAID is salicylic acid, the active metabolite of aspirin, a key ingredient in many skin-care products, and part of human diets.[168] 4-amino-SA (salicylic acid) was introduced into clinical use in 1948 as an antibiotic for tuberculosis treatment[169] and is administered (PASER) to patients at a dosage of 4 g three times a day. 5-amino-SA is an NSAID administered for treatment of inflammatory bowel disease. 2,4-dihydrobenzoic acid is a metabolite found in blood plasma after drinking cranberry juice.[170] Other salicylates and anthranilates used as drugs include diflunisal, Olsa, balsalazide, olsalazine, sulfasalazine, pamoic acid, flufenamic acid and meclofenamic acid. Separate from their capabilities to treat pain and inflammation, a number of studies have found that these salicylates inhibit development of cancer,[171] and in fact we have recently shown that injectable aspirin can be used for breast cancer imaging, as its metabolite is well detected in these tumors.[172] Based on their favorable exchange properties, it is expected that several of these agents will find use on clinical 3 T scanners.

At this point, besides the above mentioned pyrimidine analogs, purine analogs and NSAIDS, label-free CEST-guided drug delivery or CEST theranostics has been demonstrated on a wide spectrum of drugs, e.g., anticancer drugs, including cytarabine,[50] decitabine,[50] azacitidine,[50] fludarabine,[50] methotrexate and pemetrexed,[50,111] melphalan,[173] Olsa,[157] porphyrins (TPPS4)[51]; NSAIDs including anthranilic acid (flufenamic acid),[174] salicylic acid[150] and aspirin[172]; the neuroprotective drug citicoline,[175] anti-viral drugs lamivudine (3TC) and emtricitabine (FTC)[176]; the cardiovascular drug acebutolol[177] and even therapeutic bacteria and viruses, including clostridium-*NT*[178] and oncolytic herpes simplex virus (HSV).[179] Collectively, these studies demonstrated the ability of CEST MRI to directly assess the efficiency of delivery and visualize the biodistribution of drugs and biologics without the need for chemical labeling. It is expected that such a label-free theranostic strategy will have an immediate clinical impact.

7 | CONCLUSIONS

As a very wide range of molecules have labile protons, it is important to understand which have suitable protons with the appropriate k_{ex} at physiologically relevant pH values and chemical shift differences with water ($\Delta\omega$). The two-pool Bloch–McConnell equations using

a long saturation pulse can be numerically solved to characterize how the CEST contrast depends on k_{ex}, $\Delta\omega$, saturation field strength (ω_1) and number of labile protons per molecule as has been mentioned previously.[62,126,180–182] In Figure 10 and Table 1 we list the k_{ex} and $\Delta\omega$ for a set of diaCEST agents tested for various medical applications. As can be seen, the chemical shift of the porphyrins including TPPS4 can be highly upfield shifted and thus has a unique feature. As we move downfield from water, there are endogenous metabolites glucose, glutamate and creatine that have a chemical shift within 3 ppm, where glutamate and creatine have labile amine group protons and glucose has labile hydroxyl group protons. Iopamidol has multiple labile protons and lies within 6 ppm from water. I45DC-diGlu also has multiple labile protons and is located further downfield. Salicylic acid and Olsa have chemical shifts closer to 10 ppm. In Figure 11, select diaCEST agents we describe in this review are inserted into a plot of Bloch simulations to demonstrate their expected relative sensitivities at two field strengths, 11.7 T and 3 T, using 3 s saturation pulses at two saturation field strengths: 4 μT and 6 μT. This is an imperfect depiction, as some agents have many more exchangeable protons (e.g., glucose has six per molecule and Olsa has two while salicylic acid has only one). Nevertheless, what can be seen is that the detection is expected to improve at the higher field strength, 11.7 T, compared with the widely clinically used 3 T. For example, for salicylic acid, Olsa and $TPPS_4$ porphyrin, the contrast improves about twofold from 3 T to 11.7 T for B_1 = 4 μT and about fourfold from 3 T to 11.7 T for B_1 = 6 μT.

For iopamidol, the contrast improves about 11-fold from 3 T to 11.7 T for 4 μT and about 37-fold from 3 T to 11.7 T for 6 μT. I45DC-diGlu, the contrast improves about threefold from 3 T to 11.7 T for 4 μT and about sevenfold from 3 T to 11.7 T for 6 μT. Even for D-glucose, creatine and glutamate, the contrast improved by larger factors with increases in B_0 and B_1. In vivo behavior is not quite so easily predicted of course, and the contrast for these small molecules will depend on the microenvironment for the tissue in which these reside, which will impact exchange and relaxation rates. These simulations only take into account direct saturation with a moderate $T_{2w} = T_{2s} = 0.1$ s and not semi-solid MT. Inclusion of MT effects may further reduce contrast, as has been described previously.[183] In fact, this dependence on microenvironment is a positive feature, as changes in environmental pH result in significant differences in contrast for any CEST pH sensor such as iopamidol or I45DC-diGlu, enabling the production of pH maps. Other important factors include pharmacokinetics of the agent and toxicity of the compounds. Based on all these considerations, different agents may perform better for each application. In terms of use of applying CEST imaging for patient studies at 3 T, endogenous compounds such as creatine and glutamate that exist at high concentration appear particularly promising. In addition, detection of sugars, triiodobenzenes, aspirin and I45DC-diGlu after administration should reveal new information for patients with cancer and with reduced kidney function, as these compounds are well tolerated and detectable on human scanners as has been described in the sections above. Indeed, the clinical feasibility of glucoCEST MRI has been demonstrated on patients with various types of brain tumor at several different sites.[184–186] In addition, a recent study also demonstrated the utility of glucoCEST MRI for characterizing Alzheimer's disease using a 3 T small animal MRI scanner.[187] These studies prove that, even for diaCEST agents such as glucose whose exchange rate falls in the

intermediate to fast regime, translation of this technology on clinical 3 T scanners is on the horizon, with new diagnostic information available as a result. On the other hand, as pointed out in the Horizon 2020 GLINT consortium report,[188] clinical translation of diaCEST agents such as glucose will still require tremendous progress, including the development of robust imaging sequences and sophisticated postprocessing algorithms, especially reliable methods for correction of motion artifacts. Multi-center, cross-vendor standardization and validation are also urgently needed. In summary, diaCEST agents appear poised to play an expanding role in diagnostic radiology moving forward.

Funding information

NIH, Grant/Award Numbers: R01DK121847-01A1, P41EB024495; AIRC, Grant/Award Number: MFAG #20153

Abbreviations:

3OMG	3-O-methyl-D-glucose
BA	barbituric acid
BAL	BA liposome
BBB	blood–brain barrier
catalyCEST	catalysis CEST
CDase	cytosine deaminase
CEST	chemical exchange saturation transfer
CT	computed tomography
diaCEST	diamagnetic CEST
FDG	18F-fluoro-2-deoxy-2-D-glucose
GEST	guest exchange saturation transfer
GluCEST	glutamate CEST
glucoCEST	glucose CEST
GSH	glutathione
I45DC-diGlu	4,5-bis[(Glu)carbonyl]-1H-imidazole
kex	chemical exchange rates
MTRasym	asymmetric magnetization transfer ratio
NSAID	non-steroidal anti-inflammatory drug
Olsa	olsalazine
paraCEST	paramagnetic CEST

PBS	phosphate buffered saline
PET	positron emission tomography
pHe	extracellular pH
PSMA	prostate-specific membrane antigen
Δω	chemical shift differences with water
ω1	saturation field strength

REFERENCES

1. He H, Zhao K, Xiao L, et al. Detection and chiral recognition of α-hydroxyl acid through ^{1}H and CEST NMR spectroscopy using a ytterbium macrocyclic complex. Angew Chem Int Ed. 2019;58(50):18286–18289.
2. Woods M, Woessner DE, Sherry AD. Paramagnetic lanthanide complexes as PARACEST agents for medical imaging. Chem Soc Rev. 2006;35(6): 500–511. [PubMed: 16729144]
3. Dorazio SJ, Olatunde AO, Tsitovich PB, Morrow JR. Comparison of divalent transition metal ion paraCEST MRI contrast agents. J Biol Inorg Chem. 2014;19(2):191–205. [PubMed: 24253281]
4. Dastrù W, Menchise V, Ferrauto G, et al. Modulation of the prototropic exchange rate in pH-responsive Yb-HPDO3A derivatives as paraCEST agents. ChemistrySelect. 2018;3(22):6035–6041.
5. Tóth É, Bonnet CS. Responsive ParaCEST contrast agents. Inorganics. 2019;7(5):68.
6. Schröder L, Lowery TJ, Hilty C, Wemmer DE, Pines A. Molecular imaging using a targeted magnetic resonance hyperpolarized biosensor. Science. 2006;314(5798):446–449. [PubMed: 17053143]
7. Witte C, Martos V, Rose HM, et al. Live-cell MRI with xenon hyper-CEST biosensors targeted to metabolically labeled cell-surface glycans. Angew Chem Int Ed. 2015;54(9):2806–2810.
8. Yang Y, Zhang Y, Wang B, et al. Coloring ultrasensitive MRI with tunable metal–organic frameworks. Chem Sci. 2021;12(12):4300–4308. [PubMed: 34163694]
9. Zeng Q, Bie B, Guo Q, et al. Hyperpolarized Xe NMR signal advancement by metal–organic framework entrapment in aqueous solution. Proc Natl Acad Sci U S A. 2020;117(30):17558–17563. [PubMed: 32661173]
10. Shapiro MG, Ramirez RM, Sperling LJ, et al. Genetically encoded reporters for hyperpolarized xenon magnetic resonance imaging. Nat Chem. 2014; 6(7):629–634. [PubMed: 24950334]
11. Bai Y, Wang Y, Goulian M, Driks A, Dmochowski IJ. Bacterial spore detection and analysis using hyperpolarized ^{129}Xe chemical exchange saturation transfer (Hyper-CEST) NMR. Chem Sci. 2014;5(8):3197–3203. [PubMed: 25089181]
12. Dagher AP, Aletras A, Choyke P, Balaban RS. Imaging of urea using chemical exchange-dependent saturation transfer at 1.5T. J Magn Reson Imaging. 2000;12(5):745–748. [PubMed: 11050645]
13. Wolff SD, Balaban RS. NMR imaging of labile proton-exchange. J Magn Reson. 1990;86(1):164–169.
14. Goffeney N, Bulte JW, Duyn J, Bryant LH Jr, van Zijl PC. Sensitive NMR detection of cationic-polymer-based gene delivery systems using saturation transfer via proton exchange. J Am Chem Soc. 2001;123(35):8628–8629. [PubMed: 11525684]
15. Ward KM, Aletras AH, Balaban RS. A new class of contrast agents for MRI based on proton chemical exchange dependent saturation transfer (CEST). J Magn Reson. 2000;143(1):79–87. [PubMed: 10698648]
16. Snoussi K, Bulte JW, Gueron M, van Zijl PC. Sensitive CEST agents based on nucleic acid imino proton exchange: detection of poly (rU) and of a dendrimer-poly (rU) model for nucleic acid delivery and pharmacology. Magn Reson Med. 2003;49(6):998–1005. [PubMed: 12768576]

17. Zhou J, Lal B, Wilson DA, Laterra J, van Zijl PCM. Amide proton transfer (APT) contrast for imaging of brain tumors. Magn Reson Med. 2003;50(6): 1120–1126. [PubMed: 14648559]
18. McMahon MT, Gilad AA, Bulte JWM, van Zijl PCM. Chemical Exchange Saturation Transfer Imaging: Advances and Applications. Singapore: Pan Stanford; 2017.
19. Escalona S, Blasco JA, Reza MM, Andradas E, Gómez N. A systematic review of FDG-PET in breast cancer. Med Oncol. 2010;27(1):114–129. [PubMed: 19277913]
20. Pons F, Duch J, Fuster D. Breast cancer therapy: the role of PET-CT in decision making. Q J Nucl Med Mol Imaging. 2009;53(2):210–223. [PubMed: 19293769]
21. Rivlin M, Navon G. Molecular imaging of tumors by chemical exchange saturation transfer MRI of glucose analogs. Quant Imaging Med Surg. 2019; 9(10):1731–1746. [PubMed: 31728315]
22. Walker-Samuel S, Ramasawmy R, Torrealdea F, et al. In vivo imaging of glucose uptake and metabolism in tumors. Nat Med. 2013;19(8):1067–1072. doi:10.1038/nm.3252 [PubMed: 23832090]
23. Chan KW, McMahon MT, Kato Y, et al. Natural D-glucose as a biodegradable MRI contrast agent for detecting cancer. Magn Reson Med. 2012;68(6): 1764–1773. [PubMed: 23074027]
24. Silber HE, Nyberg J, Hooker AC, Karlsson MO. Optimization of the intravenous glucose tolerance test in T2DM patients using optimal experimental design. J Pharmacokinet Pharmacodyn. 2009;36(3):281–295. [PubMed: 19554431]
25. Zaiss M, Anemone A, Goerke S, et al. Quantification of hydroxyl exchange of D-glucose at physiological conditions for optimization of glucoCEST MRI at 3, 7 and 9.4 Tesla. NMR Biomed. 2019;32(9):e4113 [PubMed: 31313865]
26. Capozza M, Anemone A, Dhakan C, et al. GlucoCEST MRI for the evaluation response to chemotherapeutic and metabolic treatments in a murine triple-negative breast cancer: a comparison with[^{18}F]F-FDG-PET. Mol Imaging Biol. 2022;24(1):126–134. doi:10.1007/s11307-021-01637-6 [PubMed: 34383241]
27. Rivlin M, Tsarfaty I, Navon G. Functional molecular imaging of tumors by chemical exchange saturation transfer MRI of 3-*O*-methyl-D-glucose. Magn Reson Med. 2014;72(5):1375–1380. [PubMed: 25236979]
28. Anemone A, Capozza M, Arena F, et al. In vitro and in vivo comparison of MRI chemical exchange saturation transfer (CEST) properties between native glucose and 3-*O*-methyl-D-glucose in a murine tumor model. NMR Biomed. 2021;34(12):e4602 [PubMed: 34423470]
29. Wang J, Fukuda M, Chung JJ, Wang P, Jin T. Chemical exchange sensitive MRI of glucose uptake using xylose as a contrast agent. Magn Reson Med. 2021;85(4):1953–1961. [PubMed: 33107108]
30. Jin T, Mehrens H, Wang P, Kim SG. Glucose metabolism-weighted imaging with chemical exchange-sensitive MRI of 2-deoxyglucose (2DG) in brain: sensitivity and biological sources. NeuroImage. 2016;143:82–90. [PubMed: 27570111]
31. Bagga P, Wilson N, Rich L, et al. Sugar alcohol provides imaging contrast in cancer detection. Sci Rep. 2019;9(1):11092. [PubMed: 31366892]
32. Haris M, Cai K, Singh A, Hariharan H, Reddy R. In vivo mapping of brain myo-inositol. NeuroImage. 2011;54(3):2079–2085. [PubMed: 20951217]
33. Chan KW, Jiang L, Cheng M, et al. CEST-MRI detects metabolite levels altered by breast cancer cell aggressiveness and chemotherapy response. NMR Biomed. 2016;29(6):806–816. [PubMed: 27100284]
34. Liu G, Moake M, Har-el Y-e, et al. In vivo multicolor molecular MR imaging using diamagnetic chemical exchange saturation transfer liposomes. Magn Reson Med. 2012;67(4):1106–1113. [PubMed: 22392814]
35. Cai K, Haris M, Singh A, et al. Magnetic resonance imaging of glutamate. Nat Med. 2012;18(2):302–306. [PubMed: 22270722]
36. Jin T, Autio J, Obata T, Kim SG. Spin-locking versus chemical exchange saturation transfer MRI for investigating chemical exchange process between water and labile metabolite protons. Magn Reson Med. 2011;65(5):1448–1460. [PubMed: 21500270]
37. Bagga P, Crescenzi R, Krishnamoorthy G, et al. Mapping the alterations in glutamate with GluCEST MRI in a mouse model of dopamine deficiency. J Neurochem. 2016;139(3):432–439. [PubMed: 27529288]

38. Cai KJ, Singh A, Roalf DR, et al. Mapping glutamate in subcortical brain structures using high-resolution GluCEST MRI. NMR Biomed. 2013;26(10): 1278–1284. [PubMed: 23553932]
39. Hadar PN, Kini LG, Nanga RPR, et al. Volumetric glutamate imaging (GluCEST) using 7T MRI can lateralize nonlesional temporal lobe epilepsy: a preliminary study. Brain Behav. 2021;11(8):e02134 [PubMed: 34255437]
40. Demetriou E, Tachrount M, Zaiss M, Shmueli K, Golay X. PRO-QUEST: a rapid assessment method based on progressive saturation for quantifying exchange rates using saturation times in CEST. Magn Reson Med. 2018;80(4):1638–1654. [PubMed: 29504144]
41. Chan KWY, Liu G, Song X, et al. MRI-detectable pH nanosensors incorporated into hydrogels for in vivo sensing of transplanted-cell viability. Nat Mater. 2013;12(3):268–275. [PubMed: 23353626]
42. Haris M, Nanga RP, Singh A, et al. Exchange rates of creatine kinase metabolites: feasibility of imaging creatine by chemical exchange saturation transfer MRI. NMR Biomed. 2012;25(11):1305–1309. [PubMed: 22431193]
43. Kogan F, Haris M, Singh A, et al. Method for high-resolution imaging of creatine in vivo using chemical exchange saturation transfer. Magn Reson Med. 2013. doi:10.1002/mrm.24641:n/a-n/a
44. Chen L, Barker PB, Weiss RG, van Zijl PCM, Xu J. Creatine and phosphocreatine mapping of mouse skeletal muscle by a polynomial and Lorentzian line-shape fitting CEST method. Magn Reson Med. 2019;81(1):69–78. [PubMed: 30246265]
45. Rerich E, Zaiss M, Korzowski A, Ladd ME, Bachert P. Relaxation-compensated CEST-MRI at 7T for mapping of creatine content and pH—preliminary application in human muscle tissue in vivo. NMR Biomed. 2015;28(11):1402–1412. [PubMed: 26374674]
46. Jiang W, Zhou IY, Wen L, Zhou X, Sun PZ. A theoretical analysis of chemical exchange saturation transfer echo planar imaging (CEST-EPI) steady state solution and the CEST sensitivity efficiency-based optimization approach. Contrast Media Mol Imaging. 2016;11(5):415–423. [PubMed: 27312932]
47. Pavuluri K, Rosenberg JT, Helsper S, Bo S, McMahon MT. Amplified detection of phosphocreatine and creatine after supplementation using CEST MRI at high and ultrahigh magnetic fields. J Magn Reson. 2020;313:106703. [PubMed: 32179431]
48. Liu G, Liang Y, Bar-Shir A, et al. Monitoring enzyme activity using a diamagnetic chemical exchange saturation transfer magnetic resonance imaging contrast agent. J Am Chem Soc. 2011;133(41):16326–16329. [PubMed: 21919523]
49. Han Z, Li Y, Zhang J, et al. Molecular imaging of deoxycytidine kinase activity using deoxycytidine-enhanced CEST MRI. Cancer Res. 2019;79(10): 2775–2783. [PubMed: 30940660]
50. Li Y, Chen H, Xu J, et al. CEST theranostics: label-free MR imaging of anticancer drugs. Oncotarget. 2016;7(6):6369–6378. [PubMed: 26837220]
51. Zhang X, Yuan Y, Li S, et al. Free-base porphyrins as CEST MRI contrast agents with highly upfield shifted labile protons. Magn Reson Med. 2019; 82(2):577–585. [PubMed: 30968442]
52. Chakraborty S, Das M, Srinivasan A, Ghosh A. Tetrakis-(*N*-methyl-4-pyridinium)-porphyrin as a diamagnetic chemical exchange saturation transfer (diaCEST) MRI contrast agent. New J Chem. 2021;45(3):1262–1268.
53. Vahrmeijer AL, Hutteman M, van der Vorst JR, van de Velde CJ, Frangioni JV. Image-guided cancer surgery using near-infrared fluorescence. Nat Rev Clin Oncol. 2013;10(9):507–518. [PubMed: 23881033]
54. Pushpan SK, Venkatraman S, Anand VG, et al. Porphyrins in photodynamic therapy—a search for ideal photosensitizers. Curr Med Chem Anticancer Agents. 2002;2(2):187–207. [PubMed: 12678743]
55. Longo DL, Moustaghfir FZ, Zerbo A, et al. EXCI-CEST: exploiting pharmaceutical excipients as MRI-CEST contrast agents for tumor imaging. Int J Pharm. 2017;525(1):275–281. [PubMed: 28433532]
56. Yang X, Song X, Li Y, et al. Salicylic acid and analogs: diamagnetic chemical exchange satuation transfer (diaCEST) magnetic resonance imaging (MRI) contrast agents with highly shifted exchangeable protons. Angew Chem Int Ed. 2013. doi:10.1002/anie.201302764

57. Song X, Yang X, Ray Banerjee S, Pomper MG, McMahon MT. Anthranilic acid analogues as diamagnetic CEST (diaCEST) MRI contrast agents that feature an IntraMolecular-bond Shifted HYdrogen (IM-SHY). Contrast Media Mol Imaging. 2014. doi:10.1002/cmmi.1597
58. Li J, Feng X, Zhu W, et al. Chemical exchange saturation transfer (CEST) agents: quantum chemistry and MRI. Chemistry. 2016;22(1):264–271. [PubMed: 26616530]
59. Dang T, Suchy M, Truong YJ, et al. Hydrazo-CEST: hydrazone-dependent chemical exchange saturation transfer magnetic resonance imaging contrast agents. Chemistry. 2018;24(36):9148–9156. [PubMed: 29645309]
60. Brun EMSP-T, Calvert ND, Suchý M, et al. Mapping vitamin B 6 metabolism by hydrazoCEST magnetic resonance imaging. Chem Commun. 2021; 57(83):10867–10870.
61. Chakraborty S, Peruncheralathan S, Ghosh A. Paracetamol and other acetanilide analogs as inter-molecular hydrogen bonding assisted diamagnetic CEST MRI contrast agents. RSC Adv. 2021;11(12):6526–6534. [PubMed: 35423188]
62. Yang X, Yadav NN, Song XL, et al. Tuning phenols with Intra-Molecular Bond Shifted HYdrogens (IM-SHY) as diaCEST MRI contrast agents. Chemistry. 2014;20(48):15824–15832. [PubMed: 25302635]
63. McDonald RJ, McDonald JS, Bida JP, et al. Intravenous contrast material-induced nephropathy: causal or coincident phenomenon? Radiology. 2013; 267(1):106–118. [PubMed: 23360742]
64. Orbeck H. Bilateral renal cortical necrosis and general Schwartzman reaction. Literature review and case presentation. Tidsskr Nor Laegeforening. 1971;91(16):1222–1225.
65. Gillies RJ, Raghunand N, Garcia-Martin ML, Gatenby RA. pH imaging. IEEE Eng Med Biol Mag. 2004;23(5):57–64.
66. Gillies RJ, Raghunand N, Karczmar GS, Bhujwalla ZM. MRI of the tumor microenvironment. J Magn Reson Imaging. 2002;16(4):430–450. [PubMed: 12353258]
67. Pavuluri K, McMahon MT. pH imaging using chemical exchange saturation transfer (CEST) MRI. Israel J Chem. 2017;57(9):862–879.
68. Aime S, Nano R, Grandi M. A new class of contrast agents for magnetic resonance imaging based on selective reduction of water-T2 by chemical exchange. Invest Radiol. 1988;23(Suppl 1):S267–S270. [PubMed: 3198360]
69. Aime S, Calabi L, Biondi L, et al. Iopamidol: exploring the potential use of a well-established x-ray contrast agent for MRI. Magn Reson Med. 2005; 53(4):830–834. [PubMed: 15799043]
70. Longo DL, Dastrù W, Digilio G, et al. Iopamidol as a responsive MRI–chemical exchange saturation transfer contrast agent for pH mapping of kidneys: in vivo studies in mice at 7 T. Magn Reson Med. 2011;65(1):202–211. [PubMed: 20949634]
71. Sun PZ, Longo DL, Hu W, Xiao G, Wu R. Quantification of iopamidol multi-site chemical exchange properties for ratiometric chemical exchange saturation transfer (CEST) imaging of pH. Phys Med Biol. 2014;59(16):4493–4504. [PubMed: 25054859]
72. Longo DL, Sun PZ, Consolino L, Michelotti FC, Uggeri F, Aime S. A general MRI-CEST ratiometric approach for pH imaging: demonstration of in vivo pH mapping with iobitridol. J Am Chem Soc. 2014;136(41):14333–14336. [PubMed: 25238643]
73. Chen LQ, Howison CM, Jeffery JJ, Robey IF, Kuo PH, Pagel MD. Evaluations of extracellular pH within in vivo tumors using acidoCEST MRI. Magn Reson Med. 2014;72(5):1408–1417. [PubMed: 24281951]
74. Moon BF, Jones KM, Chen LQ, et al. A comparison of iopromide and iopamidol, two acidoCEST MRI contrast media that measure tumor extracellular pH. Contrast Media Mol Imaging. 2015;10(6):446–455. [PubMed: 26108564]
75. Wu Y, Zhou IY, Igarashi T, Longo DL, Aime S, Sun PZ. A generalized ratiometric chemical exchange saturation transfer (CEST) MRI approach for mapping renal pH using iopamidol. Magn Reson Med. 2018;79(3):1553–1558. [PubMed: 28686805]
76. Arena F, Irrera P, Consolino L, Colombo Serra S, Zaiss M, Longo DL. Flip-angle based ratiometric approach for pulsed CEST-MRI pH imaging. J Magn Reson. 2018;287:1–9. [PubMed: 29272735]
77. Cobb JG, Xie J, Li K, Gochberg DF, Gore JC. Exchange-mediated contrast agents for spin-lock imaging. Magn Reson Med. 2012;67(5):1427–1433. [PubMed: 21954094]

78. Longo DL, Michelotti F, Consolino L, et al. In vitro and in vivo assessment of nonionic iodinated radiographic molecules as chemical exchange saturation transfer magnetic resonance imaging tumor perfusion agents. Invest Radiol. 2016;51(3):155–162. [PubMed: 26460826]
79. Aime S, Caravan P. Biodistribution of gadolinium-based contrast agents, including gadolinium deposition. J Magn Reson Imaging. 2009;30(6):1259–1267. [PubMed: 19938038]
80. Bennett CL, Qureshi ZP, Sartor AO, et al. Gadolinium-induced nephrogenic systemic fibrosis: the rise and fall of an iatrogenic disease. Clin Kidney J. 2012;5(1):82–88. [PubMed: 22833806]
81. Stanescu AL, Shaw DW, Murata N, et al. Brain tissue gadolinium retention in pediatric patients after contrast-enhanced magnetic resonance exams: pathological confirmation. Pediatr Radiol. 2020;50(3):388–396. [PubMed: 31989188]
82. Murata N, Gonzalez-Cuyar LF, Murata K, et al. Macrocyclic and other non-group 1 gadolinium contrast agents deposit low levels of gadolinium in brain and bone tissue: preliminary results from 9 patients with normal renal function. Invest Radiol. 2016;51(7):447–453. [PubMed: 26863577]
83. Bussi S, Coppo A, Celeste R, et al. Macrocyclic MR contrast agents: evaluation of multiple-organ gadolinium retention in healthy rats. Insights Imaging. 2020;11(1):11. [PubMed: 32020385]
84. Quattrocchi CC, Mallio CA, Errante Y, et al. Gadodiamide and dentate nucleus T1 hyperintensity in patients with meningioma evaluated by multiple follow-up contrast-enhanced magnetic resonance examinations with no systemic interval therapy. Invest Radiol. 2015;50(7):470–472. [PubMed: 25756685]
85. Anemone A, Consolino L, Longo DL. MRI-CEST assessment of tumour perfusion using X-ray iodinated agents: comparison with a conventional Gd-based agent. Eur Radiol. 2017;27(5):2170–2179. [PubMed: 27572810]
86. Garcia-Martin ML, Herigault G, Remy C, et al. Mapping extracellular pH in rat brain gliomas in vivo by H-1 magnetic resonance spectroscopic imaging: comparison with maps of metabolites. Cancer Res. 2001;61(17):6524–6531. [PubMed: 11522650]
87. Provent P, Benito M, Hiba B, et al. Serial in vivo spectroscopic nuclear magnetic resonance Imaging of lactate and extracellular pH in rat gliomas shows redistribution of protons away from sites of glycolysis. Cancer Res. 2007;67(16):7638–7645. [PubMed: 17699768]
88. Yang X, Song X, Ray Banerjee S, et al. Developing imidazoles as CEST MRI pH sensors. Contrast Media Mol Imaging. 2016;11(4):304–312. [PubMed: 27071959]
89. Lauzon CB, van Zijl P, Stivers JT. Using the water signal to detect invisible exchanging protons in the catalytic triad of a serine protease. J Biomol NMR. 2011;50(4):299–314. [PubMed: 21809183]
90. Bachovchin WW. Contributions of NMR spectroscopy to the study of hydrogen bonds in serine protease active sites. Magn Reson Chem. 2001;39: S199–S213.
91. Rush JR, Sandstrom SL, Yang JQ, et al. Intramolecular hydrogen bond strength and pK_a determination of N,N′-disubstituted imidazole-4,-5-dicarboxamides. Org Lett. 2005;7(1):135–138. [PubMed: 15624996]
92. Baures PW, Rush JR, Wiznycia AV, Desper J, Helfrich BA, Beatty AM. Intramolecular hydrogen bonding and intermolecular dimerization in the crystal structures of imidazole-4,5-dicarboxylic acid derivatives. Cryst Growth Des. 2002;2(6):653–664.
93. Kirichek LT. Pharmacological activity and toxicity of neurotropic agents in experimental hypodynamia. Farmakol Toksikol. 1979;42(3):221–225. [PubMed: 446700]
94. Kniga M. Central actions of Imidazolecarboxylic acid derivatives. Farmakol Toksikol. 1959;22:11–20. [PubMed: 13653118]
95. Li Y, Qiao Y, Chen H, et al. Characterization of tumor vascular permeability using natural dextrans and CEST MRI. Magn Reson Med. 2018;79(2): 1001–1009. [PubMed: 29193288]
96. Liu G, Ray Banerjee S, Yang X, et al. A dextran-based probe for the targeted magnetic resonance imaging of tumours expressing prostate-specific membrane antigen. Nat Biomed Eng. 2017;1(12):977–982. [PubMed: 29456877]
97. van Zijl PC, Jones CK, Ren J, Malloy CR, Sherry AD. MRI detection of glycogen in vivo by using chemical exchange saturation transfer imaging (glycoCEST). Proc Natl Acad Sci U S A. 2007;104(11):4359–4364. [PubMed: 17360529]
98. Zhou Y, van Zijl PCM, Xu X, et al. Magnetic resonance imaging of glycogen using its magnetic coupling with water. Proc Natl Acad Sci U S A. 2020; 117(6):3144–3149. [PubMed: 32001509]

99. Consolino L, Irrera P, Romdhane F, Anemone A, Longo DL. Investigating plasma volume expanders as novel macromolecular MRI-CEST contrast agents for tumor contrast-enhanced imaging. Magn Reson Med. 2021;86(2):995–1007. [PubMed: 33764575]
100. Han Z, Liu G. Sugar-based biopolymers as novel imaging agents for molecular magnetic resonance imaging. Wiley Interdiscip Rev Nanomed Nanobiotechnol. 2019;11(4):e1551. [PubMed: 30666829]
101. Chen H, Liu D, Li Y, et al. CEST MRI monitoring of tumor response to vascular disrupting therapy using high molecular weight dextrans. Magn Reson Med. 2019;82(4):1471–1479. [PubMed: 31106918]
102. Han Z, Chen C, Xu X, et al. Dynamic contrast-enhanced CEST MRI using a low molecular weight dextran. NMR Biomed. 2022;35(2):e4649. doi:10.1002/nbm.4649 [PubMed: 34779550]
103. Han Z, Zhang S, Fujiwara K, et al. Extradomain-B fibronectin-targeted dextran-based chemical exchange saturation transfer magnetic resonance imaging probe for detecting pancreatic cancer. Bioconjug Chem. 2019;30(5):1425–1433. [PubMed: 30938983]
104. Zhou Y, van Zijl PCM, Xu J, Yadav NN. Mechanism and quantitative assessment of saturation transfer for water-based detection of the aliphatic protons in carbohydrate polymers. Magn Reson Med. 2021;85(3):1643–1654. [PubMed: 32970889]
105. Chan KW, Yu T, Qiao Y, et al. A diaCEST MRI approach for monitoring liposomal accumulation in tumors. J Control Release. 2014;180:51–59. [PubMed: 24548481]
106. Yu T, Chan KW, Anonuevo A, et al. Liposome-based mucus-penetrating particles (MPP) for mucosal theranostics: demonstration of diamagnetic chemical exchange saturation transfer (diaCEST) magnetic resonance imaging (MRI). Nanomedicine. 2015;11(2):401–405. [PubMed: 25461289]
107. Han X, Huang J, To AKW, et al. CEST MRI detectable liposomal hydrogels for multiparametric monitoring in the brain at 3T. Theranostics. 2020;10(5): 2215–2228. [PubMed: 32089739]
108. Demetriou E, Story HE, Bofinger R, Hailes HC, Tabor AB, Golay X. Effect of liposomal encapsulation on the chemical exchange properties of diamagnetic CEST agents. J Phys Chem B. 2019;123(35):7545–7557. [PubMed: 31449408]
109. Liu H, Jablonska A, Li Y, et al. Label-free CEST MRI detection of citicoline-liposome drug delivery in ischemic stroke. Theranostics. 2016;6(10): 1588–1600. [PubMed: 27446492]
110. Chen Z, Li Y, Airan R, et al. CT and CEST MRI bimodal imaging of the intratumoral distribution of iodinated liposomes. Quant Imaging Med Surg. 2019;9(9):1579–1591. [PubMed: 31667143]
111. Lock LL, Li Y, Mao X, et al. One-component supramolecular filament hydrogels as theranostic label-free magnetic resonance imaging agents. ACS Nano. 2017;11(1):797–805. [PubMed: 28075559]
112. Jin T, Nicholls FJ, Crum WR, Ghuman H, Badylak SF, Modo M. Diamagnetic chemical exchange saturation transfer (diaCEST) affords magnetic resonance imaging of extracellular matrix hydrogel implantation in a rat model of stroke. Biomaterials. 2017;113:176–190. [PubMed: 27816001]
113. Lesniak WG, Oskolkov N, Song X, et al. Salicylic acid conjugated dendrimers are a tunable, high performance CEST MRI nanoplatform. Nano Lett. 2016;16(4):2248–2253. [PubMed: 26910126]
114. Gilad AA, McMahon MT, Walczak P, et al. Artificial reporter gene providing MRI contrast based on proton exchange. Nat Biotechnol. 2007;25(2): 217–219. [PubMed: 17259977]
115. McMahon MT, Gilad AA, DeLiso MA, Berman SM, Bulte JW, van Zijl PC. New “multicolor” polypeptide diamagnetic chemical exchange saturation transfer (DIACEST) contrast agents for MRI. Magn Reson Med. 2008;60(4):803–812. [PubMed: 18816830]
116. Gatenby RA, Gillies RJ. Why do cancers have high aerobic glycolysis? Nat Rev Cancer. 2004;4(11):891–899. [PubMed: 15516961]
117. Aime S, Delli Castelli D, Fedeli F, Terreno E. A paramagnetic MRI-CEST agent responsive to lactate concentration. J Am Chem Soc. 2002;124(32): 9364–9365. [PubMed: 12167018]
118. Aime S, Barge A, Delli Castelli D, et al. Paramagnetic lanthanide (III) complexes as pH-sensitive chemical exchange saturation transfer (CEST) contrast agents for MRI applications. Magn Reson Med. 2002;47(4):639–648. [PubMed: 11948724]

119. Wu YK, Soesbe TC, Kiefer GE, Zhao PY, Sherry AD. A responsive europium (III) chelate that provides a direct readout of pH by MRI. J Am Chem Soc. 2010;132(40):14002–14003. [PubMed: 20853833]
120. Delli Castelli D, Terreno E, Aime S. Yb-III-HPDO3A: a dual pH- and temperature-responsive CEST agent. Angew Chem Int Ed. 2011;50(8):1798–1800.
121. Sheth VR, Li YG, Chen LQ, Howison CM, Flask CA, Pagel MD. Measuring in vivo tumor pHe with CEST-FISP MRI. Magn Reson Med. 2012;67(3): 760–768. [PubMed: 22028287]
122. McVicar N, Li AX, Suchy M, Hudson RHE, Menon RS, Bartha R. Simultaneous in vivo pH and temperature mapping using a PARACEST-MRI contrast agent. Magn Reson Med. 2013;70(4):1016–1025. [PubMed: 23165779]
123. Castelli DD, Ferrauto G, Cutrin JC, Terreno E, Aime S. In vivo maps of extracellular pH in murine melanoma by CEST-MRI. Magn Reson Med. 2014; 71(1):326–332. [PubMed: 23529973]
124. Ward KM, Balaban RS. Determination of pH using water protons and chemical exchange dependent saturation transfer (CEST). Magn Reson Med. 2000;44(5):799–802. [PubMed: 11064415]
125. Zhou J, Payen JF, Wilson DA, Traystman RJ, van Zijl PCM. Using the amide proton signals of intracellular proteins and peptides to detect pH effects in MRI. Nat Med. 2003;9(8):1085–1090. [PubMed: 12872167]
126. McMahon MT, Gilad AA, Zhou J, Sun PZ, Bulte JW, van Zijl PC. Quantifying exchange rates in chemical exchange saturation transfer agents using the saturation time and saturation power dependencies of the magnetization transfer effect on the magnetic resonance imaging signal (QUEST and QUESP): pH calibration for poly-L-lysine and a starburst dendrimer. Magn Reson Med. 2006;55(4):836–847. [PubMed: 16506187]
127. Sun PZ, Benner T, Kumar A, Sorensen AG. Investigation of optimizing and translating pH-sensitive pulsed-chemical exchange saturation transfer (CEST) imaging to a 3T clinical scanner. Magn Reson Med. 2008;60(4):834–841. [PubMed: 18816867]
128. Wang H, Wang L, Zhang H, et al. ^{1}H NMR-based metabolic profiling of human rectal cancer tissue. Mol Cancer. 2013;12(1):121. [PubMed: 24138801]
129. Chen LQ, Howison CM, Jeffery JJ, Robey IF, Kuo PH, Pagel MD. Evaluations of extracellular pH within in vivo tumors using acidoCEST MRI. Magn Reson Med. 2013. doi:10.1002/mrm.25053:n/a-n/a
130. Ibrahim-Hashim A, Estrella V. Acidosis and cancer: from mechanism to neutralization. Cancer Metastasis Rev. 2019;38(1/2):149–155. [PubMed: 30806853]
131. Vaupel P, Schmidberger H, Mayer A. The Warburg effect: essential part of metabolic reprogramming and central contributor to cancer progression. Int J Radiat Biol. 2019;95(7):912–919. [PubMed: 30822194]
132. Longo DL, Bartoli A, Consolino L, et al. In vivo imaging of tumor metabolism and acidosis by combining PET and MRI-CEST pH imaging. Cancer Res. 2016;76(22):6463–6470. [PubMed: 27651313]
133. Pillai SR, Damaghi M, Marunaka Y, Spugnini EP, Fais S, Gillies RJ. Causes, consequences, and therapy of tumors acidosis. Cancer Metastasis Rev. 2019;38(1/2):205–222. [PubMed: 30911978]
134. Anemone A, Consolino L, Conti L, et al. In vivo evaluation of tumour acidosis for assessing the early metabolic response and onset of resistance to dichloroacetate by using magnetic resonance pH imaging. Int J Oncol. 2017;51(2):498–506. [PubMed: 28714513]
135. Goldenberg JM, Cárdenas-Rodríguez J, Pagel MD. Preliminary results that assess metformin treatment in a preclinical model of pancreatic cancer using simultaneous [^{18}F]FDG PET and acidoCEST MRI. Mol Imaging Biol. 2018;20(4):575–583. [PubMed: 29374343]
136. Anemone A, Consolino L, Conti L, et al. Tumour acidosis evaluated in vivo by MRI-CEST pH imaging reveals breast cancer metastatic potential. Br J Cancer. 2021;124(1):207–216. [PubMed: 33257841]
137. Wu H, Estrella V, Beatty M, et al. T-cells produce acidic niches in lymph nodes to suppress their own effector functions. Nat Commun. 2020;11(1): 4113 [PubMed: 32807791]
138. Jones KM, Randtke EA, Yoshimaru ES, et al. Clinical translation of tumor acidosis measurements with acidoCEST MRI. Mol Imaging Biol. 2017;19(4): 617–625. [PubMed: 27896628]

139. Longo DL, Busato A, Lanzardo S, Antico F, Aime S. Imaging the pH evolution of an acute kidney injury model by means of iopamidol, a MRI-CEST pH-responsive contrast agent. Magn Reson Med. 2013;70(3):859–864. [PubMed: 23059893]
140. Longo DL, Cutrin JC, Michelotti F, Irrera P, Aime S. Noninvasive evaluation of renal pH homeostasis after ischemia reperfusion injury by CEST-MRI. NMR Biomed. 2017;30(7):e3720.
141. Irrera P, Consolino L, Cutrin JC, Zöllner FG, Longo DL. Dual assessment of kidney perfusion and pH by exploiting a dynamic CEST-MRI approach in an acute kidney ischemia–reperfusion injury murine model. NMR Biomed. 2020;33(6):e4287 [PubMed: 32153058]
142. Pavuluri K, Manoli I, Pass A, et al. Noninvasive monitoring of chronic kidney disease using pH and perfusion imaging. Sci Adv. 2019;5(8):eaaw8357. [PubMed: 31453331]
143. Müller-Lutz A, Khalil N, Schmitt B, et al. Pilot study of iopamidol-based quantitative pH imaging on a clinical 3T MR scanner. Magn Reson Mater Phys Biol Med. 2014;27(6):477–485.
144. Bo S, Sedaghat F, Pavuluri K, et al. Dynamic contrast enhanced-MR CEST urography: an emerging tool in the diagnosis and management of upper urinary tract obstruction. Tomography. 2021;7(1):80–94. [PubMed: 33801533]
145. Airan RD, Bar-Shir A, Liu G, et al. MRI biosensor for protein kinase A encoded by a single synthetic gene. Magn Reson Med. 2012;68(6):1919–1923. [PubMed: 23023588]
146. Jamin Y, Eykyn TR, Poon E, Springer CJ, Robinson SP. Detection of the prodrug-activating enzyme carboxypeptidase G2 activity with chemical exchange saturation transfer magnetic resonance. Mol Imaging Biol. 2014;16(2):152–157. [PubMed: 23955100]
147. Haris M, Singh A, Mohammed I, et al. In vivo magnetic resonance imaging of tumor protease activity. Sci Rep. 2014;4:6081. [PubMed: 25124082]
148. Bar-Shir A, Liu G, Liang Y, et al. Transforming thymidine into a magnetic resonance imaging probe for monitoring gene expression. J Am Chem Soc. 2013;135(4):1617–1624. [PubMed: 23289583]
149. Bar-Shir A, Liu G, Greenberg MM, Bulte JW, Gilad AA. Synthesis of a probe for monitoring HSV1-tk reporter gene expression using chemical exchange saturation transfer MRI. Nat Protoc. 2013;8(12):2380–2391. [PubMed: 24177294]
150. Yang X, Song X, Li Y, et al. Salicylic acid and analogues as diaCEST MRI contrast agents with highly shifted exchangeable proton frequencies. Angew Chem Int Ed Engl. 2013;52(31):8116–8119. [PubMed: 23794432]
151. Daryaei I, Ghaffari MM, Jones KM, Pagel MD. Detection of alkaline phosphatase enzyme activity with a catalyCEST MRI biosensor. ACS Sens. 2016; 1(7):857–861. [PubMed: 30246144]
152. Fernandez-Cuervo G, Sinharay S, Pagel MD. A catalyCEST MRI contrast agent that can simultaneously detect two enzyme activities. Chembiochem. 2016;17(5):383–387. [PubMed: 26693680]
153. Hingorani DV, Montano LA, Randtke EA, Lee YS, Cardenas-Rodriguez J, Pagel MD. A single diamagnetic catalyCEST MRI contrast agent that detects cathepsin B enzyme activity by using a ratio of two CEST signals. Contrast Media Mol Imaging. 2016;11(2):130–138. [PubMed: 26633584]
154. Sinharay S, Howison CM, Baker AF, Pagel MD. Detecting in vivo urokinase plasminogen activator activity with a catalyCEST MRI contrast agent. NMR Biomed. 2017;30(7):e3721.
155. Sinharay S, Randtke EA, Jones KM, et al. Noninvasive detection of enzyme activity in tumor models of human ovarian cancer using catalyCEST MRI. Magn Reson Med. 2017;77(5):2005–2014. [PubMed: 27221386]
156. Sinharay S, Randtke EA, Howison CM, Ignatenko NA, Pagel MD. Detection of enzyme activity and inhibition during studies in solution, in vitro and in vivo with catalyCEST MRI. Mol Imaging Biol. 2018;20(2):240–248. [PubMed: 28726131]
157. Yuan Y, Zhang J, Qi X, et al. Furin-mediated intracellular self-assembly of olsalazine nanoparticles for enhanced magnetic resonance imaging and tumour therapy. Nat Mater. 2019;18(12):1376–1383. [PubMed: 31636420]
158. Yadav NN, Yang X, Li Y, Li W, Liu G, van Zijl PCM. Detection of dynamic substrate binding using MRI. Sci Rep. 2017;7(1):10138. [PubMed: 28860625]

159. Tirukoti ND, Avram L, Haris T, et al. Fast ion-chelate dissociation rate for in vivo MRI of labile zinc with frequency-specific encodability. J Am Chem Soc. 2021;143(30):11751–11758. [PubMed: 34297566]
160. Goren E, Avram L, Bar-Shir A. Versatile non-luminescent color palette based on guest exchange dynamics in paramagnetic cavitands. Nat Commun. 2021;12(1). doi:10.1038/s41467-021-23179-9
161. Avram L, Havel V, Shusterman-Krush R, et al. Dynamic interactions in synthetic receptors: a guest exchange saturation transfer study. Chemistry. 2018. doi:10.1002/chem.201805973
162. Avram L, Bar-Shir A. ^{19}F-GEST NMR: studying dynamic interactions in host–guest systems. Organ Chem Front. 2019;6(9):1503–1512.
163. Chen XS. Introducing Theranostics journal—from the editor-in-chief. Theranostics. 2011;1:1–2. [PubMed: 21547150]
164. Choi KY, Liu G, Lee S, Chen X. Theranostic nanoplatforms for simultaneous cancer imaging and therapy: current approaches and future perspectives. Nanoscale. 2012;4(2):330–342. [PubMed: 22134683]
165. Shi J, Kantoff PW, Wooster R, Farokhzad OC. Cancer nanomedicine: progress, challenges and opportunities. Nat Rev Cancer. 2017;17(1):20–37. [PubMed: 27834398]
166. Blau R, Krivitsky A, Epshtein Y, Satchi-Fainaro R. Are nanotheranostics and nanodiagnostics-guided drug delivery stepping stones towards precision medicine? Drug Resist Updat. 2016;27:39–58. [PubMed: 27449597]
167. Han X, Lai JHC, Huang J, Park SW, Liu Y, Chan KWY. Imaging self-healing hydrogels and chemotherapeutics using CEST MRI at 3 T. ACS Appl Bio Mater. 2021;4(7):5605–5616.
168. Paterson JR, Baxter G, Dreyer JS, Halket JM, Flynn R, Lawrence JR. Salicylic acid sans aspirin in animals and man: persistence in fasting and biosynthesis from benzoic acid. J Agric Food Chem. 2008;56(24):11648–11652. [PubMed: 19053387]
169. Lehmann J. Para-aminosalicylic acid in the treatment of tuberculosis. Lancet. 1946;250(JAN5):15–16.
170. Zhang K, Zuo Y. GC-MS Determination of flavonoids and phenolic and benzoic acids in human plasma after consumption of cranberry juice. J Agric Food Chem. 2004;52(2):222–227. [PubMed: 14733499]
171. Rainsford K, Day R, Hicks M, et al. (Eds). Aspirin and Related Drugs. CRC Press; 2004.
172. Pavuluri K, Yang E, Ayyappan V, et al. Unlabeled aspirin as an activatable theranostic MRI agent for breast cancer. Theranostics. 2022;12(4): 1937–1951. doi:10.7150/thno.53147 [PubMed: 35198081]
173. Ngen EJ, Bar-Shir A, Jablonska A, et al. Imaging the DNA alkylator melphalan by CEST MRI: an advanced approach to theranostics. Mol Pharm. 2016; 13(9):3043–3053. [PubMed: 27398883]
174. Song X, Yang X, Ray Banerjee S, Pomper MG, McMahon MT. Anthranilic acid analogs as diamagnetic CEST MRI contrast agents that feature an intramolecular-bond shifted hydrogen. Contrast Media Mol Imaging. 2015;10(1):74–80. [PubMed: 24771546]
175. Grieb P. Neuroprotective properties of citicoline: facts, doubts and unresolved issues. CNS Drugs. 2014;28(3):185–193. [PubMed: 24504829]
176. Bade AN, Gendelman HE, McMillan J, Liu Y. Chemical exchange saturation transfer for detection of antiretroviral drugs in brain tissue. AIDS. 2021; 35(11):1733–1741. [PubMed: 34049358]
177. Fenniche S, Dhaoui A, Ammar FB, Benmously R, Marrak H, Mokhtar I. Acebutolol-induced subacute cutaneous lupus erythematosus. Skin Pharmacol Physiol. 2005;18(5):230–233. [PubMed: 16015021]
178. Liu G, Bettegowda C, Qiao Y, et al. Noninvasive imaging of infection after treatment with tumor-homing bacteria using Chemical Exchange Saturation Transfer (CEST) MRI. Magn Reson Med. 2013;70(6):1690–1698. [PubMed: 24123389]
179. Farrar CT, Buhrman JS, Liu G, et al. Establishing the lysine-rich protein CEST reporter gene as a CEST MR imaging detector for oncolytic virotherapy. Radiology. 2015;275(3):746–754. [PubMed: 25686366]

180. Zaiss M, Angelovski G, Demetriou E, McMahon MT, Golay X, Scheffler K. QUESP and QUEST revisited—fast and accurate quantitative CEST experiments. Magn Reson Med. 2018;79(3):1708–1721. [PubMed: 28686796]

181. Randtke EA, Chen LQ, Corrales LR, Pagel MD. The Hanes-Woolf linear QUESP method improves the measurements of fast chemical exchange rates with CEST MRI. Magn Reson Med. 2014;71(4):1603–1612. [PubMed: 23780911]

182. Dixon WT, Ren J, Lubag AJ, et al. A concentration-independent method to measure exchange rates in PARACEST agents. Magn Reson Med. 2010; 63(3):625–632. [PubMed: 20187174]

183. Rodríguez-Rodríguez A, Zaiss M, Esteban-Gómez D, Angelovski G, Platas-Iglesias C. Paramagnetic chemical exchange saturation transfer agents and their perspectives for application in magnetic resonance imaging. Int Rev Phys Chem. 2021;40(1):51–79.

184. Bender B, Herz K, Deshmane A, et al. GLINT: GlucoCEST in neoplastic tumors at 3 T—clinical results of GlucoCEST in gliomas. Magn Reson Mater Phys Biol Med. 2021. doi:10.1007/s10334-021-00982-5

185. Xu X, Sehgal AA, Yadav NN, et al. D-glucose weighted chemical exchange saturation transfer (glucoCEST)-based dynamic glucose enhanced (DGE) MRI at 3T: early experience in healthy volunteers and brain tumor patients. Magn Reson Med. 2020;84(1):247–262. [PubMed: 31872916]

186. Herz K, Lindig T, Deshmane A, et al. $T_1\rho$-based dynamic glucose-enhanced (DGEρ) MRI at 3 T: method development and early clinical experience in the human brain. Magn Reson Med. 2019;82(5):1832–1847. [PubMed: 31231853]

187. Huang J, van Zijl PCM, Han X, et al. Altered D-glucose in brain parenchyma and cerebrospinal fluid of early Alzheimer's disease detected by dynamic glucose-enhanced MRI. Sci Adv. 2020;6(20):eaba3884. [PubMed: 32426510]

188. Kim M, Eleftheriou A, Ravotto L, et al. What do we know about dynamic glucose-enhanced (DGE) MRI and how close is it to the clinics? Horizon 2020 GLINT Consortium Report. Magn Reson Mater Phys Biol Med. 2022. doi:10.1007/s10334-021-00994-1

189. Jin T, Mehrens H, Hendrich KS, Kim SG. Mapping brain glucose uptake with chemical exchange-sensitive spin-lock magnetic resonance imaging. J Cereb Blood Flow Metab. 2014;34(8):1402–1410. [PubMed: 24865996]

190. Cui J, Zu Z. Towards the molecular origin of glutamate CEST (GluCEST) imaging in rat brain. Magn Reson Med. 2020;83(4):1405–1417. [PubMed: 31691367]

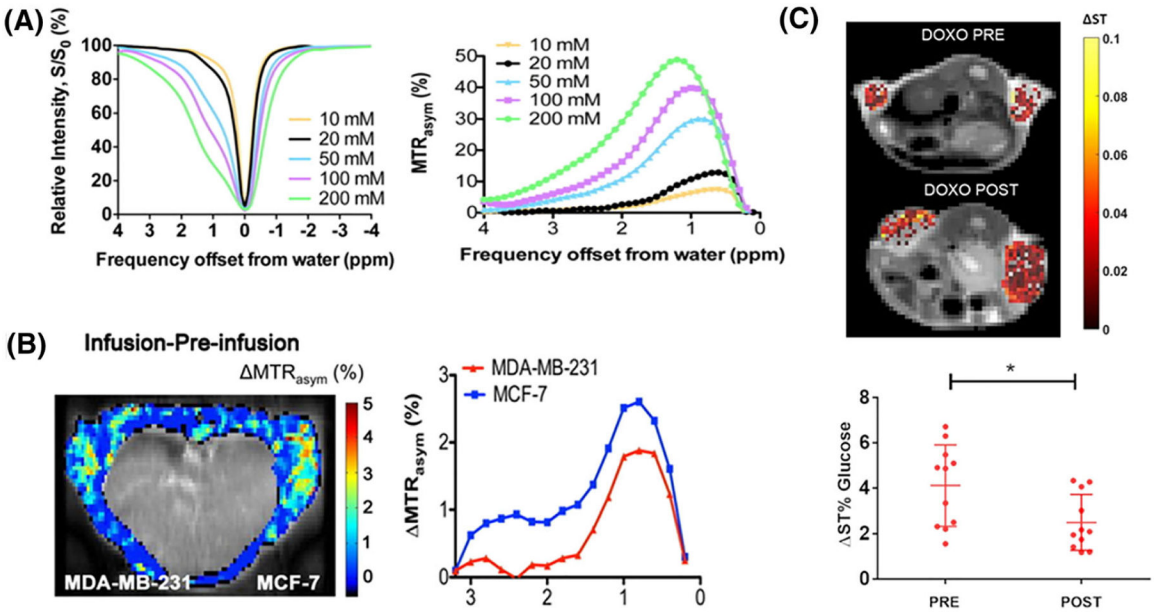

FIGURE 1.

A, *Z*-spectra (left) and MTR_{asym} (right) as a function of concentration at pH 7.3 for B_1 = 1.6 μT. B, Left: GlucoCEST difference map, $\Delta MTR_{asym} = MTR_{asym}(\text{infusion}) - MTR_{asym}(\text{pre-infusion})$. The intensity of the internal body was thresholded out because it contains moving areas (lungs and heart) that have large magnetic susceptibility differences from surrounding tissues, which complicates difference imaging. Right: the ΔMTR_{asym} profiles of MDA-MB-231 and MCF-7. [Reprinted with permission from Reference 23] C, Top: representative glucoCEST ΔST% maps of 4T1 tumor-bearing mice, before and after treatment. Data are reported as the difference (ΔST%) between the ST effect before and after the intravenous glucose injection. Parametric maps are superimposed on T_{2w} anatomical images, and glucoCEST contrast is shown only in the tumor region. Bottom: graph showing individual GlucoCEST contrast (and mean ± SD) obtained injecting glucose at a 3 g/kg dose via intravenous bolus (n = 6 mice). Data are reported as the variation (ΔST%) between the ST effect post-injection and the ST effect pre-injection. Paired t-test *p = 0.0216. (Reprinted with permission from Reference 26)

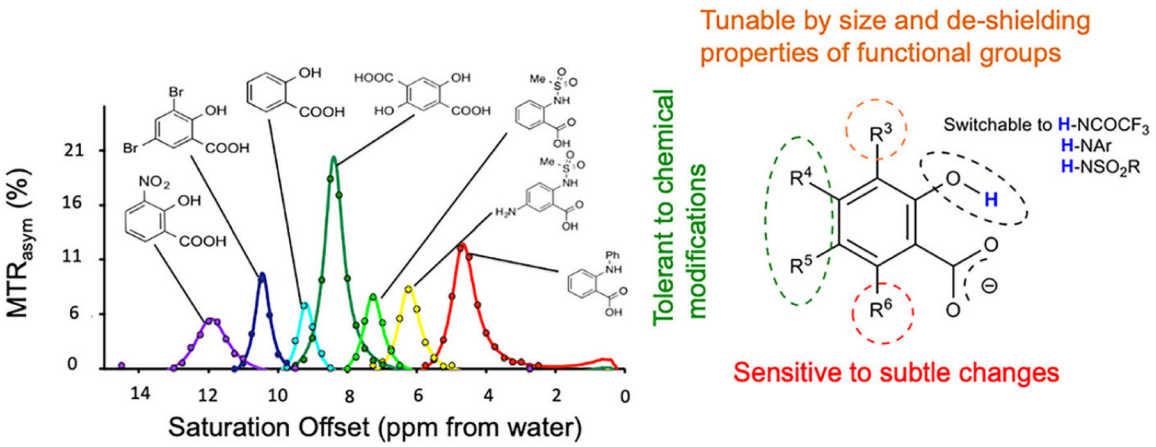

FIGURE 2.

Select salicylate and anthranilate CEST agents. A, Seven of these agents with labile protons resonating between 5 and 12 ppm from water; B, general scaffold for these agents, with MRI properties tolerant to conjugation at R4, R5. (Reprinted from Reference 62)

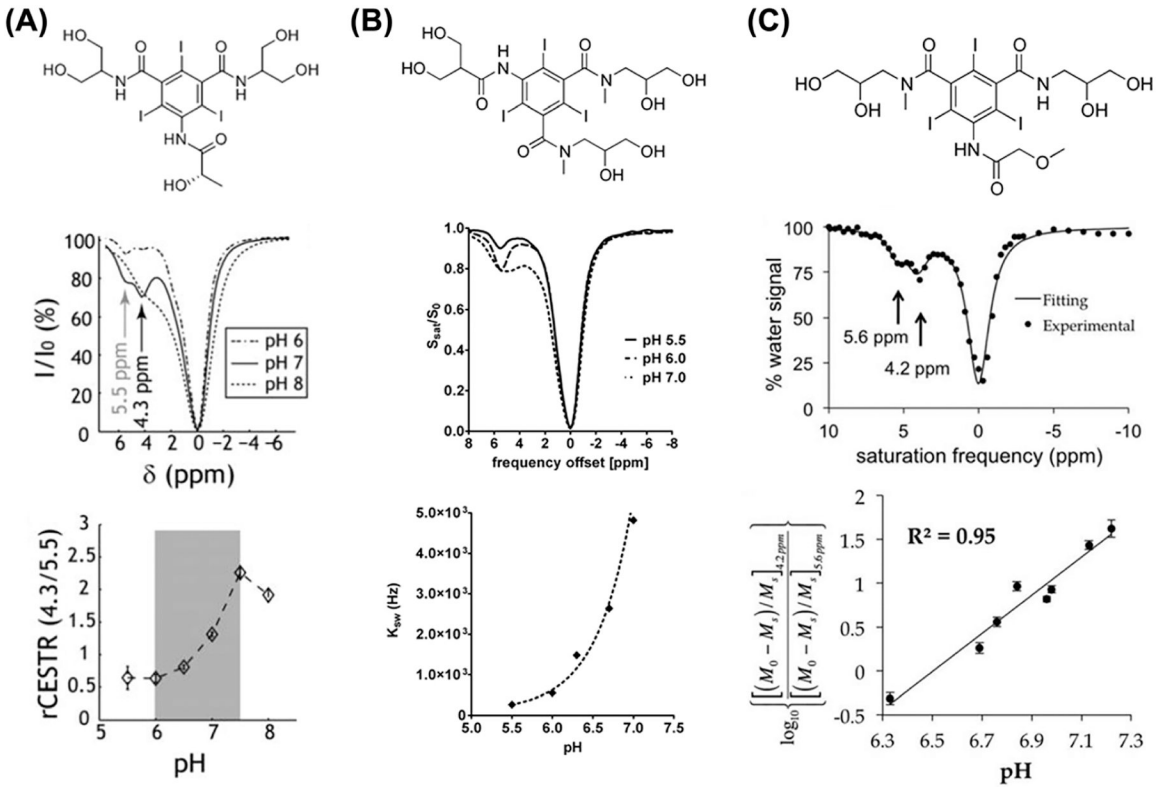

FIGURE 3.

Comparison between iopamidol, iobitridol and iopromide ratiometric pH MRI. A, Top: iopamidol chemical structure. Middle: *z*-spectra for representative pH values of 6, 7 and 8 (B_1 = 2.5 μT, TS = 5 s) at room temperature. Bottom: ratiometric CEST analysis is sensitive to pH ranging from 6 to 7.5. (Adapted from Reference 71.) B, Top: iobitridol chemical structure with a single amide proton group. Middle: CEST spectra of 30 mM iobitridol solution at pH values of 5.5, 6.0 and 7.0. The reduction in MRI signal from bulk water signal upon selective irradiation at 5.6 ppm is pH sensitive (RF saturation power = 3 μT × 5 s, T = 310 K, B_0 = 7 T). Bottom: numerically solved pH-dependent chemical exchange rate for labile protons at 5.6 ppm. (Reprinted from Reference 72.) C, Top: the chemical structure of iopromide. Middle: a CEST spectrum of 200 mM iopromide at pH 6.69 and 37.0 °C with saturation applied at 2 μT for 5 s. Bottom: a $\log_{10}$ ratio of the two CEST effects is linearly correlated with pH from pH 6.3 to pH 7.2. (Reprinted from Reference 73)

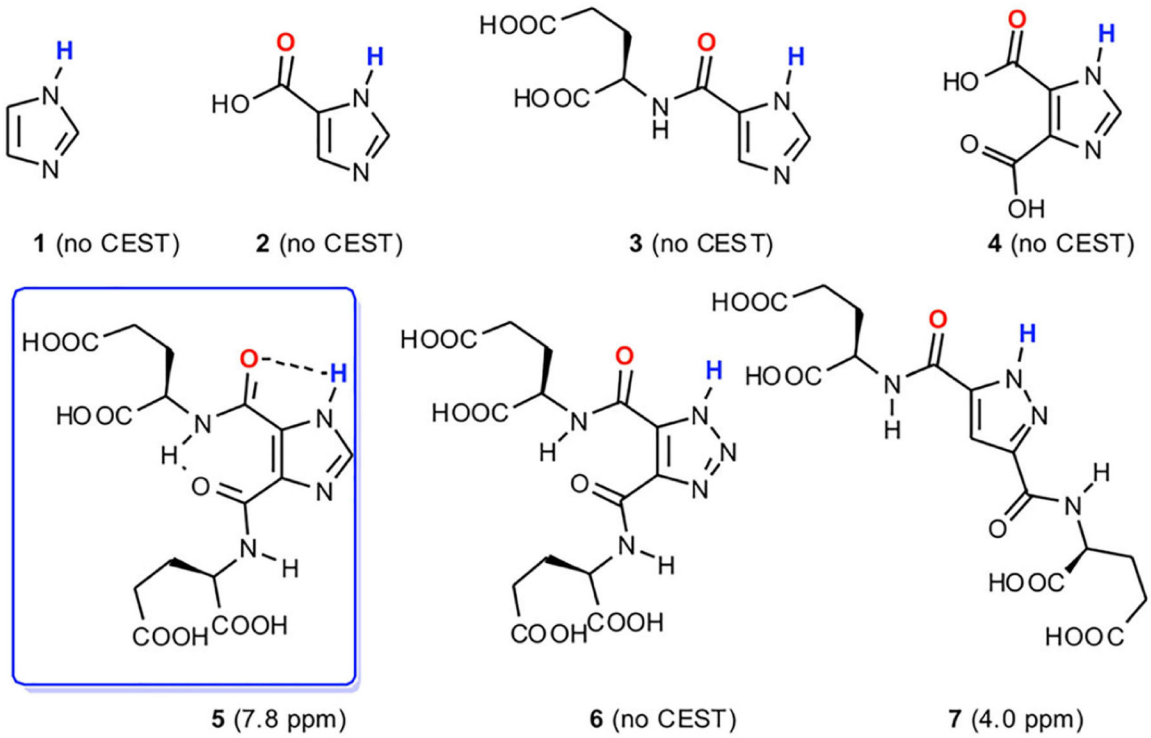

FIGURE 4.
Select azole derivatives analyzed for their CEST properties. (Reprinted from Reference 88)

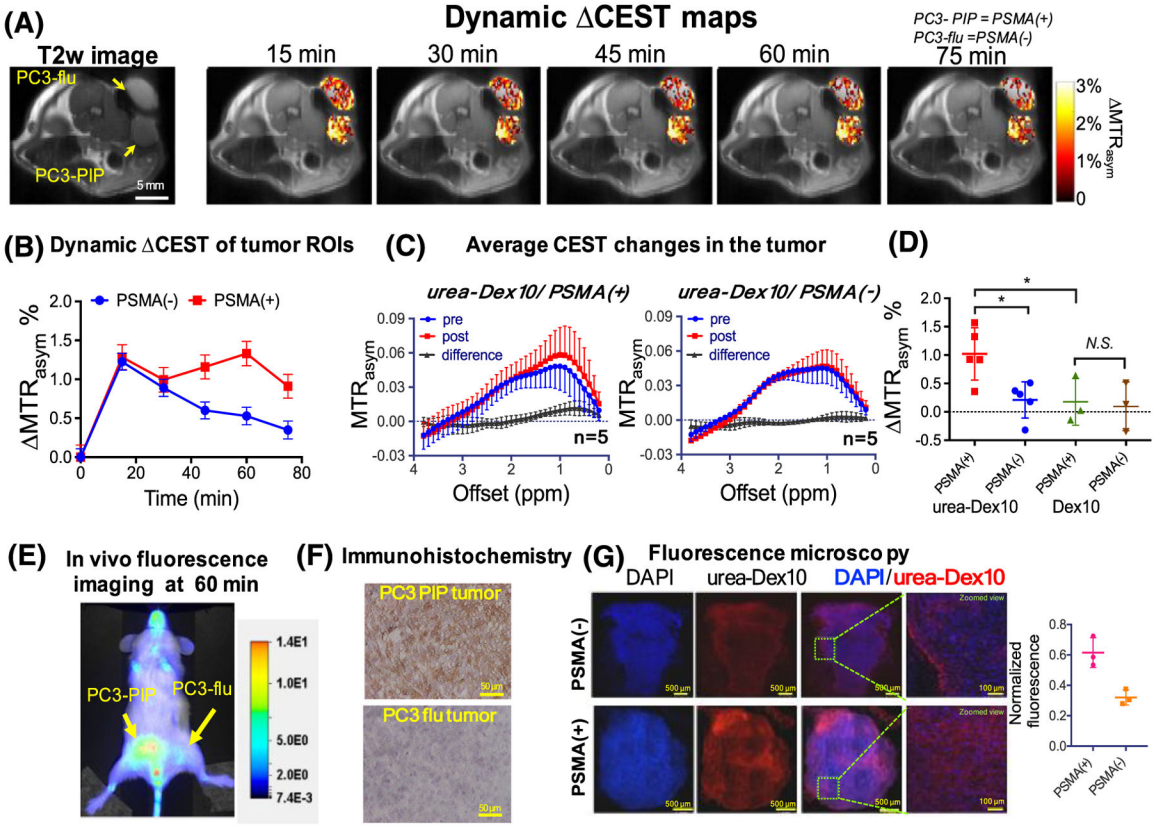

FIGURE 5.

Changes in the dynamic CEST signal in PSMA(+) and PSMA(−) tumors. A, T_2-weighted image and dynamic CEST maps at 1 ppm after the injection of 375 mg/kg urea–10 kDa dextran (injection volume = 100 μL). B, Mean changes in the CEST signal in PSMA(+) and PSMA(−) tumors in one of the mice for which time dependence was measured. CEST signal enhancement was quantified by $\Delta MTR_{asym} = MTR_{asym}(t) - MTR_{asym}(t = 0)$, where the error bars are the standard errors of the CEST signal of all the pixels in each tumor. All CEST images were acquired using a 1.8 μT and 3 s long CW pulse. C, Average CEST signal in the tumor for five mice before (blue) and one hour after (red) the injection of urea-Dex10. The signal difference is shown in black. Error bars are standard deviations of the CEST signal of all five tumors. D, Scatter plots showing the mean changes in CEST signal as quantified by ΔMTR_{asym}(1 h) in each type of tumor ($n = 5$ and 3 for urea-Dex10 and non-targeted Dex10, respectively). *$P < 0.05$ (Student's t-test, two tailed and unpaired). E, In vivo fluorescence image of a representative mouse showing a distinctive tumor uptake of urea-Dex10 at 60 min after injection. F, Sections of PSMA(+) PC3-PIP (top) and PSMA(−) PC3-flu (bottom) tumor stained with anti-PSMA. Images were acquired at ×40 magnification. G, Fluorescence microscopy of nuclei (blue, stained with DAPI) dextran (red, NIR-600 labeled). Scale bar 500 μm for the left three panels and 100 μm for the rightmost panels, which are the zoomed views of the area enclosed in the dashed green box in the image on the left. On the right, a scatter plot shows the comparison of the normalized mean fluorescence intensity of three different fields of view in the tumors. Reproduced from Reference 96

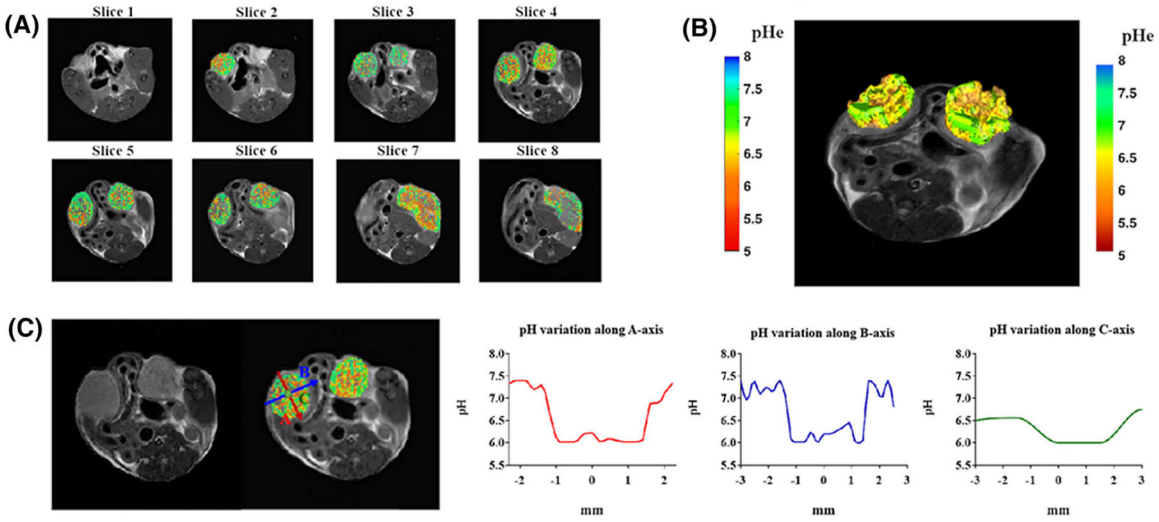

FIGURE 6.

Multislice sequence to measure pH in whole organs. A, Two-dimensional multislice tumor pH_e map for a breast tumor murine model. B, Three-dimensional pH map rendering. C, Calculated pH gradients along the three main axes inside the left tumor region showing T_2-weighted image, superimposed pH map, and pH gradients along the *A*-axis (red), *B*-axis (blue) and *C*-axis (green). (Reprinted with permission from Reference 73)

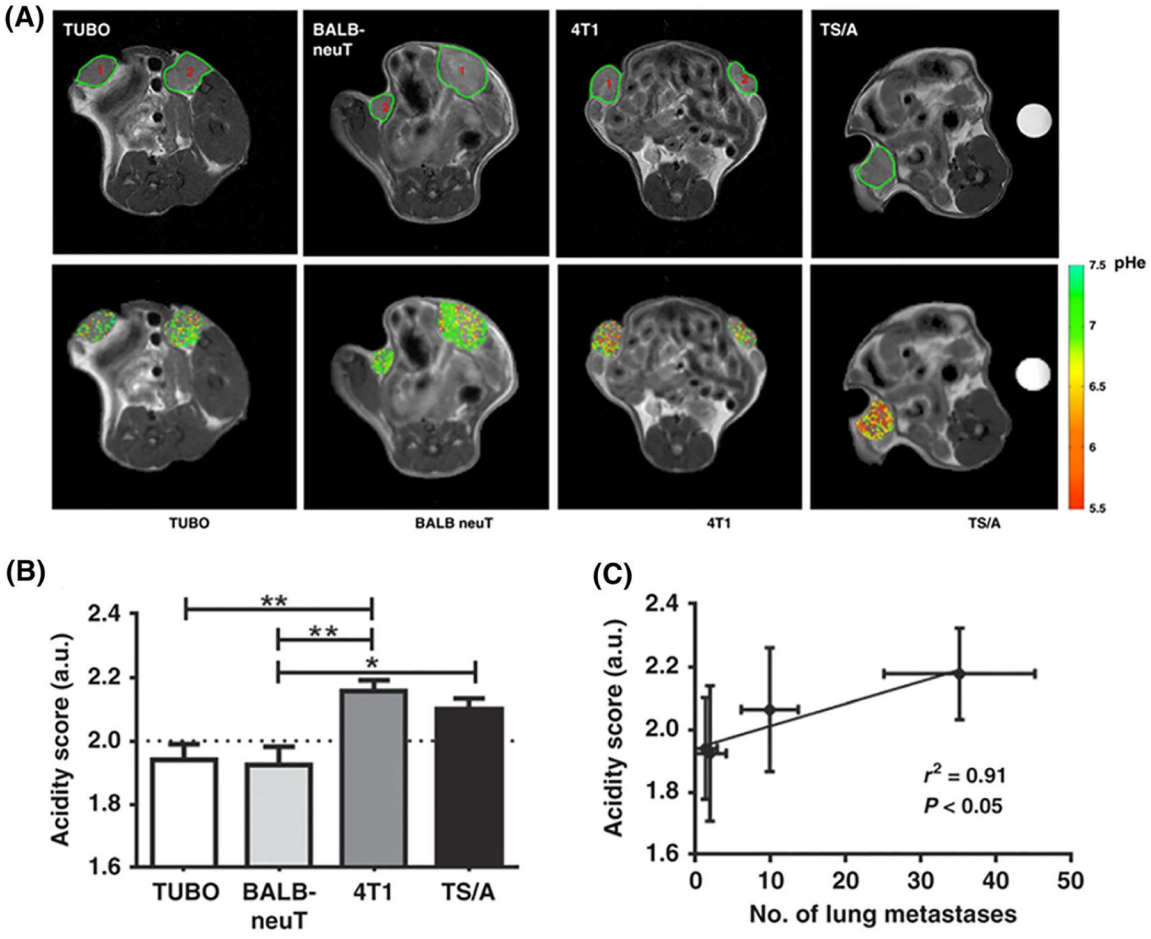

FIGURE 7.

Anatomical images of acidic tumor environment and pH_e in vivo correlation with lung metastasis. A, Top: anatomical T_{2w} images of TUBO, BALB-neuT, 4T1 and TS/A representative tumors. Bottom: representative tumor pH_e maps for TUBO, BALB-neuT, 4T1 and TS/A tumors. B, Acidity score calculated for TUBO, BALB-neuT, 4T1 and TS/A tumors. *$P < 0.05$; **$P < 0.01$. C, Correlation between acidity score and number of lung metastases ($r^2 = 0.91$, $P < 0.05$). (Reprinted with permission from Reference 136)

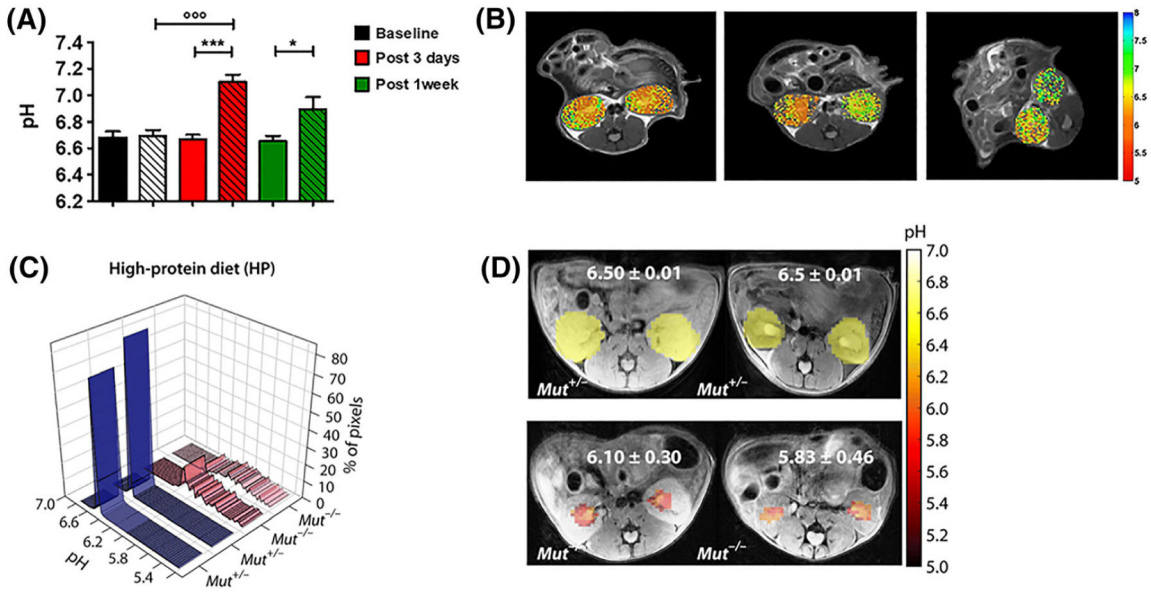

FIGURE 8.

CEST-MRI functional information about renal pH homeostasis. A, Barplots of measured CEST-MRI pH values for the whole kidneys. B, Representative pH maps (for baseline, post-3-day and post-1-week groups, respectively) superimposed onto the T_{2w} images, showing neutral pH values for the clamped kidneys. The arrow shows the clamped kidney. (*$P < 0.05$; ***$P < 0.001$; *t* test contralateral versus clamped. °°°$P < 0.001$; Bonferroni's test baseline versus clamped.) (Reprinted with permission from Reference 140.) C, pH histograms calculated for two representative HP *Mut*$^{+/-}$ mice and two representative HP *Mut*$^{-/-}$ mice. For HP *Mut*$^{+/-}$ mice more than 80% of the detected pixels display a mean pH of 6.50, whereas for HP *Mut*$^{-/-}$ mice ($n = 3$) an acidic mean pH of 6.10 to 5.83 was observed. D, Time-averaged pH images of *Mut*$^{+/-}$ and *Mut*$^{-/-}$ controls of HP mice. pH was further lowered to 5.83 for the most severely diseased mice. The pH was distributed over a narrow range of 6.50 ± 0.02 for both RD and HP *Mut*$^{+/-}$ mice, while this range significantly increased to ±0.30 and ±0.46 along with a decrease in mean pH for HP *Mut*$^{-/-}$ mice. (Reprinted with permission from Reference 142)

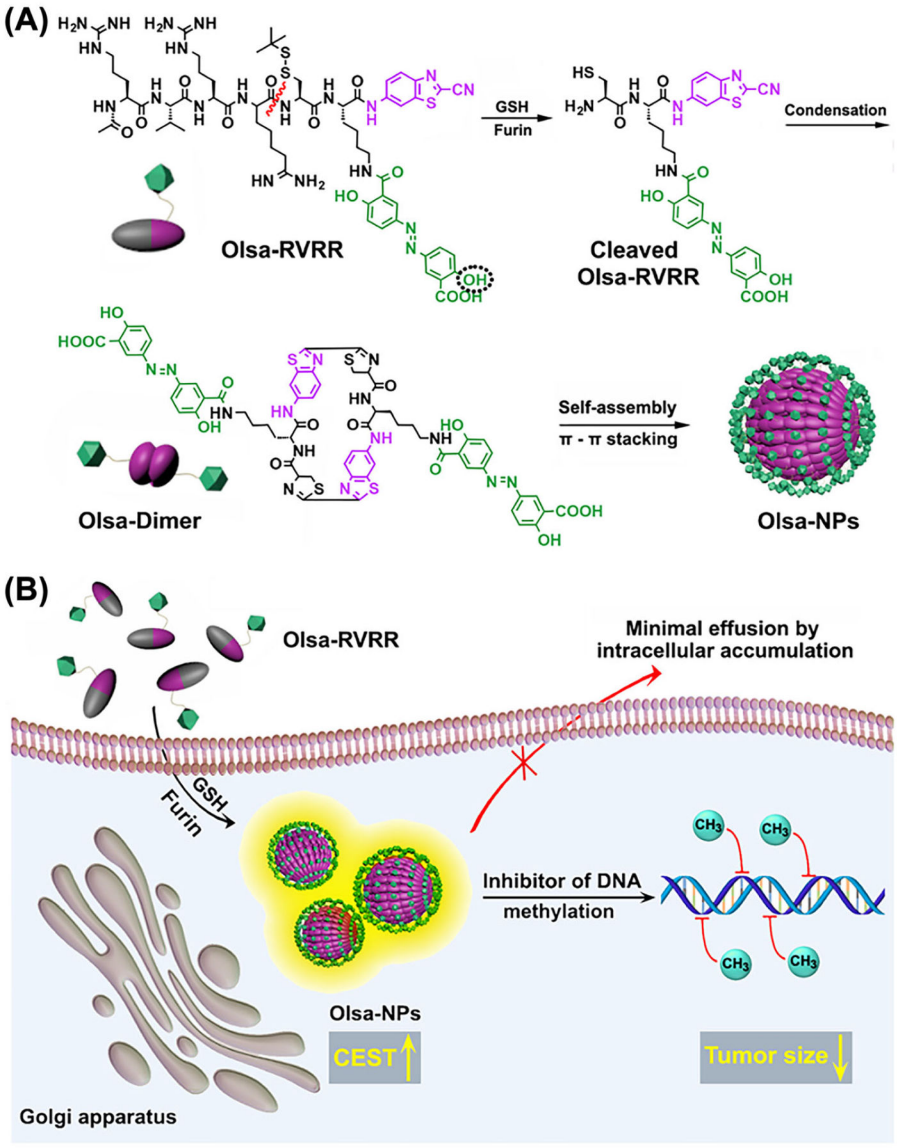

FIGURE 9.

A, Self-assembly of Olsa–RVRR into Olsa–NPs through a series of steps. The red line indicates the site of furin cleavage, and the circled hydroxyl group indicates the exchangeable hydroxyl proton that provides OlsaCEST signal at 9.8 ppm from the water frequency. B, After Olsa–RVRR enters the cytoplasm of high-furin-expressing cells (HCT116 cells in this study), it undergoes reduction by GSH and cleavage of the peptide by furin near the Golgi complex, where cleaved Olsa–RVRR is generated. Amphiphilic oligomers (mostly dimers) are then formed from the click reaction between two cleaved Olsa–RVRR molecules, followed by self-assembly into Olsa–NPs as a result of intermolecular **π**–**π** stacking. The intracellular accumulation of Olsa–NPs then serves as a reservoir of Olsa molecule enhancing CEST contrast and inhibiting DNA methylation for tumor therapy. Reprinted from Reference 157

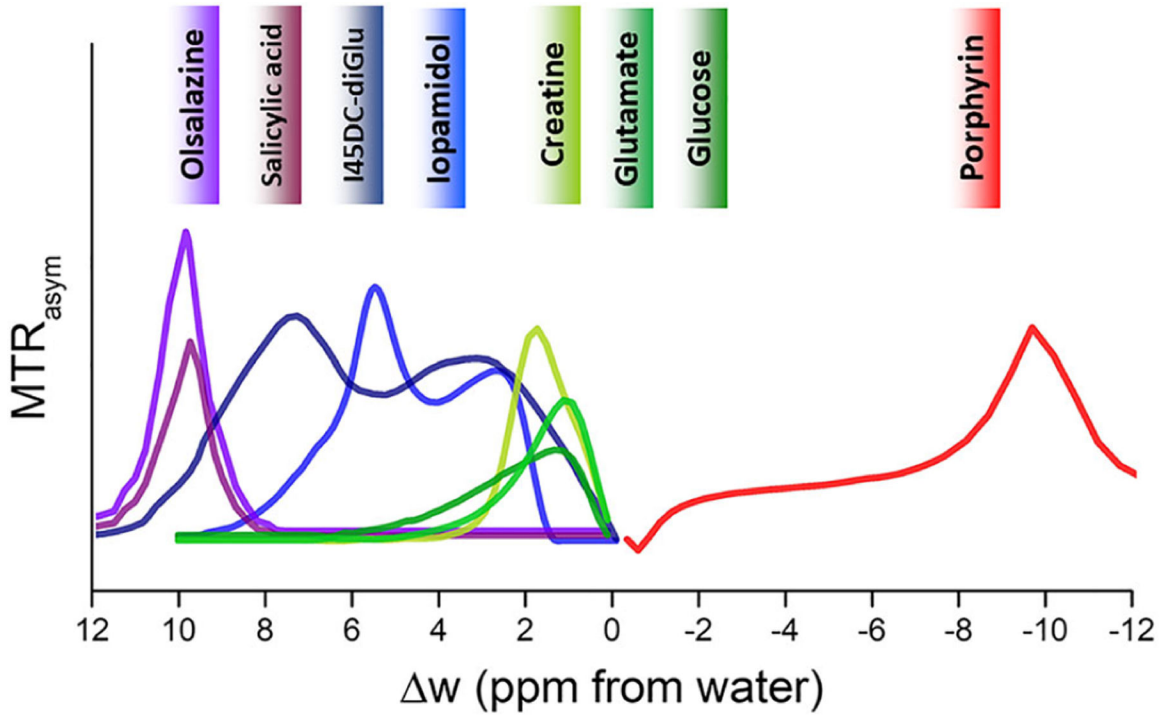

FIGURE 10.
CEST MTR_{asym} spectra for common diaCEST agents described in this review

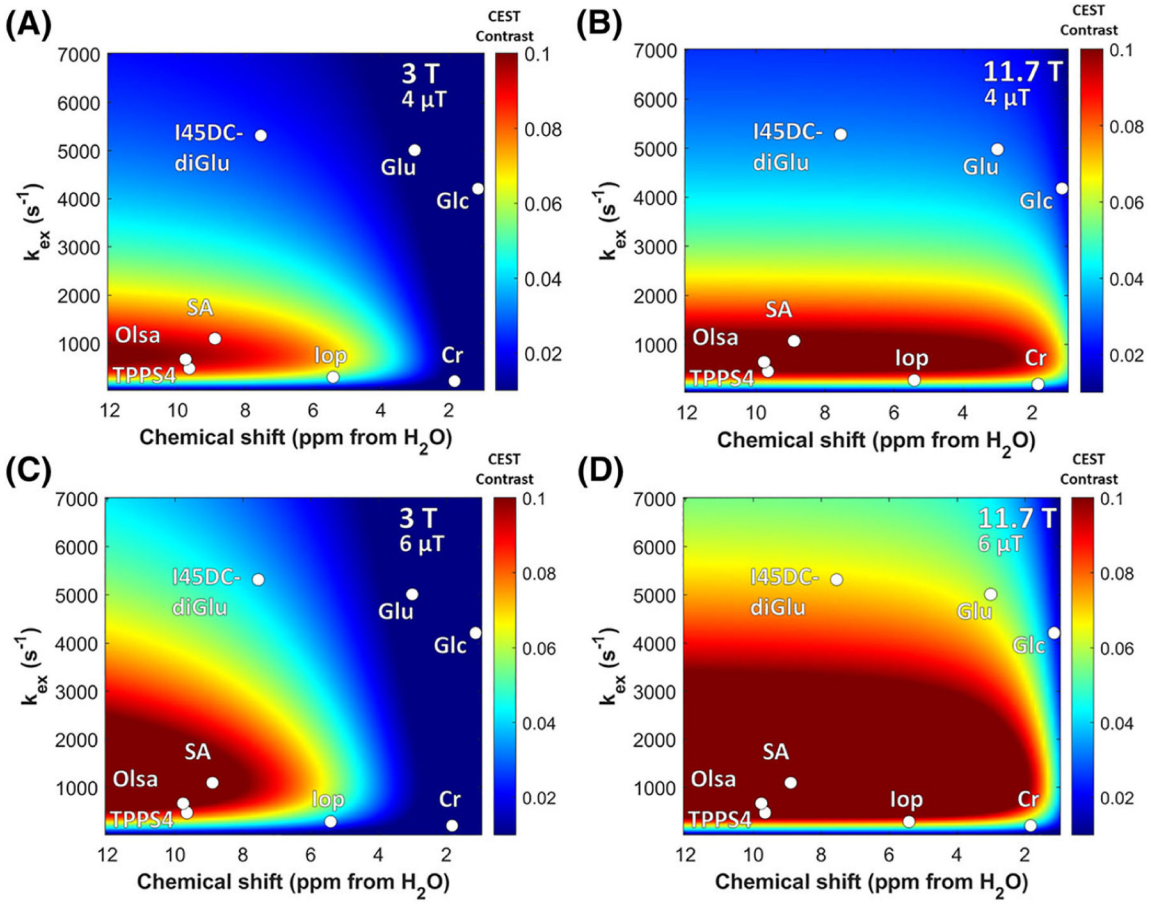

FIGURE 11.

Simulated CEST contrast as function of labile proton chemical shift $\Delta\omega$ and exchange constant k_{ex} for the following conditions: A, B_0 = 3 T, ω_1 = 4 μT; B, B_0 = 11.7 T, ω_1 = 4 μT; C, B_0 = 3 T, ω_1 = 6 μT; D, B_0 = 11.7 T, ω_1 = 6 μT. Simulation parameters: χ_{CA} = 10mM, T_{1w} = T_{1s} = 4 s, T_{2w} = T_{2s} = 0.1 s. $TPPS_4$, tetraphenylporphine sulfonate

TABLE 1

List of select diaCEST probes along with their exchange properties

diaCEST contrast agent	Concentration	B_0, B_1, t_{sat}	Chemical shifts (ppm)	T, pH	Exchange rate (s^{-1})	References
Porphyrin (TPPS4)	20 mM	9.4 T, 3.6 μT, 3 s	−9.75	37 °C, 6.6	430	[51]
D-glucose	20 mM	9.4 T, 1.6 μT, 4 s	1.2	37 °C, 6.8	4280	[189]
Glutamate	20 mM	9.4 T, 3.6 μT, 5 s	3	37 °C, 7	5000	[190]
Creatine	25 mM	11.7 T, 6 μT, 3 s	1.9	37 °C, 6.5	~175	[47]
Iopamidol	20 mM	4.7 T, 2.5 μT, 5 s	4.3, 5.5	37 °C, 6.5	265	[71]
I45DC-diGlu	25 mM	11.7 T, 5.9 μT, 3 s	4.5, 7.8	37 °C, 7.5	5300	[88]
Salicylic acid	25 mM	11.7 T, 7.2 μT, 3 s	9.3	37 °C, 7	1200	[56]
Olsa	10 mM	11.7 T, 3.6 μT, 3 s	9.8	37 °C, 7.4	697	[157]